NASA TECHNICAL NOTE

NASA TN D-6255

C.1

NASA TN D-6255

LOAN COPY: RETU
AFWL (DOGL)
KIRTLAND AFB, N

TECH LIBRARY KAFB, NM

0133027

THERMAL ANALYSIS OF CUSTOMIZED MULTILAYER INSULATION ON AN UNSHROUDED LIQUID HYDROGEN TANK

by William R. Johnson and Glenn R. Cowgill

Lewis Research Center
Cleveland, Ohio 44135

RECEIVED
12 APR 1971
Technical Library
AF Weapons
Laboratory

NATIONAL AERONAUTICS AND SPACE ADMINISTRATION • WASHINGTON, D. C. • MARCH 1971

TECH LIBRARY KAFB, NM

0133027

1. Report No. NASA TN D-6255	2. Government Accession No.	3. Recipient's
4. Title and Subtitle THERMAL ANALYSIS OF CUSTOMIZED MULTILAYER INSULATION ON AN UNSHROUDED LIQUID HYDROGEN TANK		5. Report Date March 1971
		6. Performing Organization Code
7. Author(s) William R. Johnson and Glenn R. Cowgill		8. Performing Organization Report No. E-5763
9. Performing Organization Name and Address Lewis Research Center, National Aeronautics and Space Administration, Cleveland, Ohio 44135		10. Work Unit No. 180-31
		11. Contract or Grant No.
12. Sponsoring Agency Name and Address National Aeronautics and Space Administration, Washington, D.C. 20546		13. Type of Report and Period Covered Technical Note
		14. Sponsoring Agency Code
15. Supplementary Notes		

16. Abstract

An analytical investigation was conducted to determine the space-hold thermal performance of various multilayer insulation configurations on the upper half of a liquid hydrogen tank that was continuously oriented so as to always be in the shadow of the vehicle payload. The results showed that the thermal performance achieved with a constant-thickness system can be significantly improved by varying the insulation thickness, using high-conductivity shields, and selectively increasing the surface emissivity. The degree of improvement realized was a direct function of the thermal conductivity normal to the insulation blanket.

17. Key Words (Suggested by Author(s)) Multilayer insulation; Thermal analysis; Unshrouded, sun-oriented vehicle; CINDA-3G		18. Distribution Statement Unclassified - unlimited	
19. Security Classif. (of this report) Unclassified	20. Security Classif. (of this page) Unclassified	21. No. of Pages 54	22. Price* $3.00

*For sale by the National Technical Information Service, Springfield, Virginia 22151

THERMAL ANALYSIS OF CUSTOMIZED MULTILAYER INSULATION ON AN UNSHROUDED LIQUID HYDROGEN TANK

by William R. Johnson and Glenn R. Cowgill

Lewis Research Center

SUMMARY

An analytical investigation was conducted to determine the space-hold thermal performance of various multilayer insulation (MLI) configurations on the upper half of a liquid hydrogen tank. The hypothetical vehicle assumed was sun-oriented, thus ensuring the liquid hydrogen tank to always be in the shadow of the vehicle payload. The thermal model used the geometry of a $\sqrt{2}$ oblate spheroidal tank viewing a payload simulated by a 10-foot- (3.048-m-) diameter flat disk maintained at a constant temperature of 520° R (289 K).

The results of the analysis showed that the space-hold thermal performance achieved with a conventional constant thickness of MLI can be significantly improved by

(1) Using a variable MLI thickness over the surface of the tank

(2) Using several high-lateral-thermal-conductivity shields

(3) Increasing the MLI surface emissivity in certain areas

The combination of these three items that tended to minimize the total heat flow through the MLI and into the tank was designated as the optimum configuration.

Three distinct curves expressing the local value of the effective thermal conductivity normal to the MLI blanket k_{eff} against mean temperature were used in this analysis to span the range of available experimental data. This was necessary since the absolute value of the net heat flow through the MLI and into the top half of the tank was found to be a direct function of k_{eff}.

The results of the analysis showed that the optimized configuration as previously defined reduced the net heat flows into the tank by factors of 53.84, 5.13, and 3.44 over the corresponding constant-thickness MLI configuration for the three values of k_{eff}. In addition to the improved thermal performance, the weight of the optimum configuration was approximately 71, 82, and 82 percent of the weight of the constant-thickness MLI configuration for the three values of k_{eff} used.

INTRODUCTION

The effective storage of liquid hydrogen in space can be realized by using high-performance multilayer insulation (MLI) systems. A typical system would use a large number of highly reflective shields (aluminized polyester film) separated by low-thermal-conductivity spacers (e.g., silk netting). The thermal performance of such a system approaches the ideal when the heat transfer normal to the shields approaches pure radiation.

The basic space-hold thermal performance of any MLI system, regardless of the effective thermal conductivity k_{eff} normal to the blanket of shields, can be improved by

(1) Eliminating any shroud around the liquid hydrogen tank

(2) Continuously orienting the vehicle such that the payload is always between the liquid hydrogen tank and the sun.

These two conditions thus minimize the surface area of MLI exposed to a high-temperature thermal radiation source and enable a portion of the MLI surface to reject heat directly to space.

A cross-sectional view of a sun-oriented vehicle with an unshrouded liquid hydrogen tank is shown in figure 1. The payload intercepts all solar energy and thus represents the only high-temperature heat source in the vehicle. The direction of the anticipated radiation heat flows could be as indicated by the arrows in figure 1. The only heat being transferred into any of the tanks is through the MLI on the top half of the liquid hydrogen tank, in addition to that heat transferred down the support structure itself.

The bottom half of the liquid hydrogen tank will be exposed to a combination of liquid oxygen tanks, engine, and space. The MLI surface temperatures for the liquid oxygen tanks under a space-hold condition are estimated to be extremely low. Because of these low temperatures, the heat flow from these surfaces to the liquid hydrogen tank become insignificant. Thus, the quantity of MLI on the bottom half of the liquid hydrogen tank would be determined by

(1) Ground-hold and ascent thermal protection requirements

(2) Estimated time of near-planetary operations

(3) Estimated time during mid-course corrections when the vehicle is not sun oriented

(4) Prevention of localized propellant freezing

A completely unshrouded liquid hydrogen tank is, of course, impossible to attain, since some means of supporting tankage and engine must be provided. Use of an open-strut structure will provide the minimum obstruction in maintaining the desirable space environment for the liquid hydrogen tank to view. Because of the temperature gradients and various geometric radiation view factors involved, the thermal interaction between the support structure and the MLI surface remains extremely complex to define analytically. As reported in reference 1, the number of layers, as well as the maximum shield

temperatures, determines the degree of thermal degradation obtained when the struts penetrate the MLI. Because of the unknown thermal contact resistance between the MLI and the penetration for a typical butt joint, an absolute value of this thermal degradation must be determined experimentally. Due to the complexities described, these interactions were not considered, and only the basic MLI thermal performance on the top half of the liquid hydrogen tank will be considered in this investigation.

Conceivably, the thermal performance obtained with a constant thickness of MLI can be improved upon by the use of the following concepts (shown in fig. 1):

(1) Varying the MLI thickness over the tank surface as shown, thereby permitting rejection of heat to space Q_r from surfaces at different depths within the insulation: As indicated in figure 1, the MLI edges are considered to be adiabatic surfaces, since these areas for thermal radiation are insignificant in comparison to the surface areas normal to the tank.

(2) Using high-thermal-conductivity shields (pure aluminum as opposed to aluminized mylar) to increase the lateral thermal conductivity of the MLI: This either increases the lateral heat flow Q_{lat} or decreases the temperature gradient required to transfer the same Q_{lat}, or whatever combination of these is necessary.

(3) Increasing the emissivity of those portions of the MLI surface having relatively high geometric radiation view factors to space: This increases the amount of Q_r for a given MLI surface temperature, or decreases the surface temperature required to sustain the same Q_r; or again, whatever combination of these is necessary.

Thus, the purpose of these three concepts is to laterally transfer the major portion of the heat received from the payload Q_p to the area near the side of the tank, where it can be rejected to space. The ultimate goal is to obtain as low a temperature as possible on the shield adjacent to the tank.

The objective of this analysis was to determine the effectiveness of these concepts in improving the thermal performance compared to that obtained with a conventional constant-thickness MLI system. Various configurations were evaluated to determine the optimum combination of these concepts which tended to minimize the heat flow from the payload to the upper half of the hydrogen tank.

Although the analysis is general enough for any unshrouded liquid hydrogen tank continuously oriented so as to always be in the shadow of the payload, emphasis in this investigation was with a $\sqrt{2}$ oblate spheroidal tank having a major diameter of 9.142 feet (2.786 m). This resulted in a surface area for the top half of the tank of 106.54 square feet (9.898 m^2). The tank will be in the shadow of a 10-foot- (3.048-m-) diameter flat-surfaced payload maintained at a constant temperature of 520° R (289 K). The tank-payload spacing of 0.8175 foot (0.2492 m) was estimated to be the minimum probable value attainable in an actual vehicle.

The base point of comparison will be the space-hold thermal performance using a

constant MLI thickness of 120 layers with a layer density of 50 shields per inch (19.7 shields/cm). To be consistent, the maximum number of shields used in any configuration was also arbitrarily chosen to be 120. Three distinct curves expressing the local value of k_{eff} against mean temperature were used to span the range of available experimental data. This was necessary since the absolute value of the net heat flow through the MLI and into the top half of the tank was found to be a direct function of k_{eff}. Therefore, valid comparisons of the thermal performance achieved with a constant thickness of MLI to that obtained with the optimum configuration must use several representative values for k_{eff}.

Varying the MLI thickness, in addition to possibly increasing the thermal performance, could also offer the following advantages:

(1) Reduce the MLI system weight

(2) Improve the venting capability of the MLI during the vehicle ascent, thus enabling the MLI to achieve a space-hold thermal equilibrium performance more rapidly

(3) Make the MLI system easier to fabricate and install on the tank

ANALYSIS

A cross-sectional view of a variable-thickness MLI system on the top half of the liquid hydrogen tank is shown in figure 2. The net heat flow by thermal radiation into the top surface of the MLI is transferred within the MLI by conduction in the lateral direction Q_{lat} parallel to the shields, and a combination of radiation and conduction in the normal direction Q_{norm} perpendicular to the shields. These values of interior heat transfer change with position in the MLI configuration.

For a steady-state condition to exist, the net thermal radiation received by the top surface of the MLI must be exactly equal to the total heat transferred through the MLI and into the liquid hydrogen tank itself. The net thermal radiation received by the top surface of the MLI was the algebraic summation of the individual net heat flows $q_{in,k} - q_{out,k}$ into each annular incremental surface used to make up the total surface area of the MLI covering the tank. The total heat transferred through the MLI and into the liquid hydrogen tank is the algebraic summation of the corresponding normal components of heat flow $q_{norm,k}$ across the plane adjacent to the tank surface. The net heat flow into the kth segment at the surface $q_{in,k} - q_{out,k}$ is not necessarily equal to the heat out the bottom surface $q_{norm,k}$ because lateral conduction can still exist.

The thermal performance of any given MLI configuration thus reduces to determining the MLI surface temperature profile as well as MLI interior temperatures that result in the required heat balance for steady state. A series of nodal points representing tem-

peratures throughout the MLI system, payload surface, and space were established. The existing computer program selected and then modified to simulate the physical problem and obtain a steady-state temperature distribution throughout the model was CINDA-3G (Chrysler Improved Numerical Differencing Analyzer for Third Generation Computers). The mechanics of the program, including a detailed description of all modifications and subroutines used, can be found in reference 2.

In general, the program performs a heat balance at each node and continues to adjust each temperature until an acceptable heat balance is obtained at each node. The criterion for a converged temperature profile was that the temperature change at any point be less than 0.001° R (0.00055 K) for any two consecutive iterations. Once a final temperature profile was obtained, the required heat flows between any two nodes could be readily calculated.

Thermal Radiation

An enclosure composed of the payload, the surface of the MLI, and an imaginary surface representing space is used to compute the net thermal radiation received by the top surface of the MLI. The enclosure formed with the various surfaces labeled is shown in figure 3.

The payload surface is represented by a flat disk having a diameter of 10 feet (3.048 m). The disk was arbitrarily divided into five concentric rings of approximately equal area (labeled A_{11} to A_{15} in fig. 3). Each of these five rings is considered to be a separate surface of the enclosure. Each ring is considered to be a heat source at a constant temperature of 520° R (289 K).

The use of more than one surface to represent the payload, even though the payload surface is at one constant temperature, improves the accuracy of the computed heat flows in and out of each surface when multiple reflections occur. For gray surfaces, a certain portion of the energy emitted or reflected from any particular surface may undergo multiple reflections between various other surfaces of the enclosure. Partial absorption of this energy occurs at each surface the energy is incident upon.

The emissivity of each payload surface was considered to be 0.11. This value represents the generally accepted textbook value for unpolished aluminum as stated in reference 3. Using 0.11 was conservative in that it probably represents a maximum for a real payload surface and thus maximized the quantity of heat emitted by the payload.

The MLI was arbitrarily divided into 10 annular segments from the polar cap to the equator of the tank. This was necessary in order

(1) To vary the MLI thickness over the surface of the tank (i.e., each segment represented a constant thickness)

(2) To approximate the anticipated severe temperature profile on the outer boundary of the MLI (i.e., the uniform surface temperature of any one segment may be significantly different than the uniform surface temperature of any of the other nine segments)

The emissivity specified for those surfaces requiring a high reflectivity was 0.024. This represented the experimentally determined value for aluminized mylar at ambient temperature as stated in reference 4. The emissivity specified for those surfaces where a high emissivity is desirable (targeted surfaces) was 0.9. This value of 0.9, representing the idealized value assumed for this study, can be obtained by coating the highly reflective surfaces with a high-emissivity paint. An average value of emissivity close to 0.9 can be realistically obtained as shown in references 5 to 7.

Each of these emissivities (0.024 and 0.9) was considered to be independent of temperature as a matter of convenience in simplifying the computer program input. One particular MLI configuration was rerun using emissivities of 0.015 and 0.75, respectively, to establish whether any significant change in the overall net heat flow into the tank occurred. Values of 0.015 and 0.75 were used in place of 0.024 and 0.9 since emissivity would decrease with the anticipated decreased surface temperatures over some areas of the tank.

The imaginary surface designated as space in this enclosure is the curved surface of the frustum of a right circular cone extending from the equator of the liquid hydrogen tank to the outer edge of the payload. This particular surface was assigned an absorptivity of 1 and a temperature of absolute zero. This means no energy was reflected or emitted from this surface. Since there are no reflections off this surface, there was no need for subdividing this area into smaller segments.

The net thermal radiation into each surface of the enclosure could then be determined by writing a heat balance about that particular surface. The basic assumptions used in writing the heat balance were as follows:

(1) The temperature over any given segment is uniform.

(2) All emitted and reflected energy is diffuse and uniformly distributed over an isothermal surface. Diffuse implies that the intensity is independent of direction.

(3) All surfaces are gray surfaces. Gray implies that absorptivity is equal to emissivity.

(4) Emissivity (absorptivity) and reflectivity are independent of temperature.

The following equation constitutes the heat balance for the kth surface of the enclosure:

$$q_{in,k} - q_{out,k} = q_k \tag{1}$$

where $q_{in,k}$ represents all energy (either reflected or emitted from all other surfaces)

that is intercepted by the kth surface; $q_{out,k}$ represents all energy (either directly emitted or reflected) that leaves the kth surface; and q_k then represents the net heat flow into the kth surface. (Negative q_k indicates the net heat flow is out.) For the surface simulating space $q_{out,k}$ equals zero, since both the reflectivity and the absolute temperature are set equal to zero. Thus for this surface all incident energy is absorbed (i.e., $q_k = q_{in,k}$). For any surface segment of the MLI, q_k is that heat flow which must be transferred into the MLI (or out of, as the case may be) for that particular surface.

The CINGA-3G computer program used in this analysis contains a radiosity network subroutine that computed the previously defined heat flows in terms of the surface temperatures of all segments in the enclosure. Each surface temperature thus was dependent on all other temperatures in the enclosure.

The following physical data were required by the subroutine before the matrix of equations expressing net heat flows into all segments of the enclosure could be solved:

(1) Geometric radiation view factor between any two surfaces of the enclosure. (The procedure for determining these numbers will be discussed in the following section.)

(2) Surface emissivities (either 0.024 or 0.9)

(3) Surface areas

(4) Temperatures of all surfaces

Thus, for specified temperatures on all 10 segments of the MLI, a net heat flow into the MLI is obtained.

Geometric Radiation View Factors

The geometric radiation view factor $F_{i,j}$ between the ith and j^{th} surfaces in the enclosure is defined as the fraction of energy (either emitted or reflected) leaving surface i that is intercepted by surface j. The view factor was determined between all primary surfaces in the enclosure by use of the basic definition:

$$A_i F_{i,j} = \int_{A_i}\int_{A_j} \frac{\cos \varphi_i \cos \varphi_j \, dA_i \, dA_j}{\pi R^2} \tag{2a}$$

(The symbols used are defined in the appendix.) This double integral was approximated by the following double summation in order to obtain a numerical solution on the computer:

$$A_i F_{i,j} = \sum_{A_i} \sum_{A_j} \frac{\cos \varphi_i \cos \varphi_j \, \Delta A_i \, \Delta A_j}{\pi R^2} \tag{2b}$$

A complete description of the mathematical technique used is described in appendix B of reference 2.

Use of the following two expressions then enabled all other view factors to be determined in terms of those obtained with the basic definition:

$$\sum_{k=1}^{N} F_{j,k} = 1 \tag{3}$$

where j represents any j^{th} surface and N is the number of surfaces in the enclosure.

$$A_j F_{j,k} = A_k F_{k,j} \qquad \text{(Reciprocity theorem)} \tag{4}$$

The accumulative view factor between the kth element of area on the tank surface and the entire payload can be determined from the following equation:

$$F_{k,\text{payload}} = \sum_{m=11}^{15} F_{k,m} \tag{5}$$

where $m = 11$ to 15 represents summing over the subdivided payload segments, and k simply refers to a given location on the tank surface. The relative change in $F_{k,\text{payload}}$ as a function of the location on the tank is typical of that shown in figure 4. The view factor approached zero at the side of the tank (90°), but did not equal zero since the radius of the payload was assumed to be slightly larger than the tank radius. A tank-payload spacing of 0.8175 foot (0.2492 m) and a constant MLI thickness of 120 shields were used in determining the view factors.

The view factors were determined independently for each configuration evaluated. This was necessary since the geometry including both the angular size of the segment and the number of shields (cells) at each location may change appreciably from one configuration to another.

For the variable-thickness MLI configuration, the view factors computed were slightly conservative since they did not compensate for the potential shadow of the adjoining step. This effect is illustrated in figure 5. As shown, the magnitude of the shadow

depends on the particular point on the payload being considered. Because of this varying angle, any attempt to account for this shadow becomes a very complex geometric problem. Since the ratio of the relative length of the segment being considered to the height of the adjoining step is extremely high (approx 60), the shadow effect was considered to be negligible. If not negligible, then at least the view factor generated represents the maximum, and thus simulates the highest possible heat flow from the payload to the MLI surface.

Multilayer Insulation Cells

The model used to compute the heat flow through the MLI itself was the 45° wedge portion shown in figure 6. Since the MLI is completely symmetrical over the top half of the tank, the computed thermal performance of this wedge portion was multiplied by 8 to obtain the results for the entire top half of the tank.

The 10 annular surface segments used to compute the net thermal radiation received by the MLI surface correspond to the respective surface areas of the 10 column segments of MLI. The annular surface segment is typical of that labeled normal area $A_{k,norm}$ in figure 6. Each column segment is divided into a number of constant-temperature cells, as shown in figure 6. The temperature of any given cell can then be represented by a nodal temperature located at the physical center of that particular cell. The number of cells in a given column is a function of the MLI thickness being simulated at that particular location.

As a matter of convenience in simplifying computer input, all the cells in a given column are assumed to have the same geometry (i.e., cell length and width). The dimensions of the surface cell in each column are used to determine the numerical values for the lateral cross-sectional area A_{lat}, normal area A_{norm}, and arc length L_{arc}. This assumption should introduce no significant error, since the maximum MLI thickness of 0.2 foot (6.1 cm) is small relative to the major tank diameter of 9.142 feet (2.786 m). The maximum MLI thickness is based on a nominal shield spacing of 0.020 inch (0.051 cm).

The location of the areas and arc length typical of the third column are also indicated in figure 6. The lateral cross-sectional area for those cells in the kth column $A_{k,lat}$ is determined at the junction of the k and $k + 1$ cells as the product of the partial segment circumference times the cell height. Similarly, $A_{k,norm}$ is the product of the mean partial circumference times the cell length. An average of the two cell lengths gives $L_{k,arc}$.

A typical cross section of a series of cells is shown in figure 7. Each cell contains five individual radiation shields and associated spacer materials. The shields are spaced

0.020 inch (0.051 cm) apart for a total cell height of 0.100 inch (0.254 cm). A typical cell in figure 7 has the shield positions indicated with dashed lines.

There are two different types of cells used within the MLI, the "standard" cell and the "high conductivity" cell. The "standard" cell has five shields of 0.00025-inch (0.000635-cm) mylar coated with 600 Å of aluminum on each side to give a total thickness of 0.0002547 inch (0.000647 cm). The lateral thermal conductivity k_{lat} is the weighted average of the shields and spacers over the thickness of the cell. Using a shield spacing of 0.020 inch (0.051 cm) results in

$$k_{sc,\,lat} = \frac{nw_s k_s}{n\,\Delta S} \cong \frac{k_s}{80} \tag{6}$$

In this expression k_s is the effective lateral thermal conductivity of a single shield as determined experimentally in reference 8. As a result of the way these experimental data were taken, the contribution from one spacer is included in the value of k_s.

The lateral thermal conductivity in any plane (i.e., certain vertical distance above the tank wall) can be increased by replacing one of the five double aluminized mylar shields in a cell with a shield of pure aluminum. The increased lateral thermal conductivity is thus realized at the expense of an increase in the MLI weight. Increasing the lateral thermal conductivity results in some combination or trade-off of the following two effects:

(1) Transferring more heat laterally for the same ΔT.

(2) Transferring the same quantity of heat with a much smaller ΔT.

Thus, for the plane where high lateral thermal conductivity is desired, the "standard" cell described previously is replaced by a "high conductivity" cell. In the "high conductivity" cell, one of the five aluminized mylar shields is replaced by a 0.00050 inch (0.00127 cm) shield of pure aluminum. The thickness of the pure aluminum shield is twice that of the double aluminized mylar shield in order to make the weighted average lateral thermal conductivity even higher. The weighted lateral thermal conductivity for this cell is

$$k_{hc,\,lat} = \frac{(n-1)w_s k_s + w_{al} k_{al}}{n\,\Delta S} = \frac{4(0.000254\,k_s) + 0.00050\,k_{al}}{5(0.020)} \tag{7}$$

The value of k_{al} was obtained from the bulk properties of aluminum having a purity of 99 percent. Again the value of k_s was the previously discussed experimental value. Both $k_{sc,\,lat}$ and $k_{hc,\,lat}$ were determined as a function of temperature as shown in figure 8.

As would be expected, any given plane in the MLI model must be either all "standard"

cells or all "high conductivity" cells. No mixture of the two is permitted since the model is simulating continuous sections of MLI.

The effective thermal conductivity specified in the normal direction k_{eff} as a function of temperature was valid across either a "standard" cell or a "high conductivity" cell. This is true, provided the shield spacing and spacer material are the same since the emissivity of the pure aluminum shield is the same as that for the aluminized mylar shield and since the temperature differential across either shield is negligible for the anticipated low heat-transfer rates.

With the effective thermal conductivities in both the lateral and normal directions specified, a heat balance on each individual cell can now be performed. This heat balance states that the heat added to a particular node must be exactly equal to that heat being removed from the same node for a steady-state temperature to exist. For the surface cell, the net radiation previously determined plus lateral conduction and normal conduction must add to zero. For the surface cell shown in figure 7 (which has the adiabatic surface as denoted), the equation for assumed heat flow directions becomes

$$q_{lat} + q_k = q_{norm} \tag{8}$$

$$\frac{A_{j,lat}k_{lat}(T_{j+2} - T_{k+2})}{L_{j,arc}} + q_k = \frac{A_{k,norm}k_{eff}(T_{k+2} - T_{k+1})}{n\ \Delta S} \tag{9}$$

The surface temperatures used to calculate q_k correspond to the node temperature of all of the surface cells. For the interior cell shown in figure 7, the equation becomes

$$\frac{A_{j,lat}k_{lat}(T_j - T_k)}{L_{j,arc}} + \frac{A_{k,norm}k_{eff}(T_{k+1} - T_k)}{n\ \Delta S}$$

$$= \frac{A_{k,lat}k_{lat}(T_k - T_\ell)}{L_{k,arc}} + \frac{A_{k,norm}k_{eff}(T_k - T_{k-1})}{n\ \Delta S} \tag{10}$$

After the heat balances are performed at each node within the MLI, the net heat flows out each column segment and into the tank are readily determined. The summation of these heat flows must equal the net heat received by the surface of the MLI. If the balance is not obtained, the program continues another iteration. New temperatures are "guessed" as the entire procedure is repeated. A complete description of how the computer program calculated new temperatures at each node is given in reference 2.

RESULTS AND DISCUSSION

The results and discussion section has been divided into five separate topics:

(1) The first topic, Effective Normal Thermal Conductivity, is a discussion and justification of the three values of k_{eff} used in this analysis.

(2) The second topic, Optimum Geometric Configuration, is a step-by-step discussion of how an optimum geometry was determined using a k_{eff} of 10 times pure radiation.

(3) The third topic, Thermal Effectiveness for Various Values of k_{eff}, is a comparison of the thermal effectiveness of the optimum customized configuration with the constant-MLI-thickness configuration when using different values for k_{eff}.

(4) The fourth topic, Effect of Changes in Program Variables on Thermal Performance, shows the influence of several parameters on the thermal performance for the optimum customized configuration.

(5) The fifth topic, Multilayer Insulation System Weight, presents the ratio of system weights for the optimum customized configuration to the constant-thickness MLI configuration.

Effective Normal Thermal Conductivity

The net heat flow into the tank for any MLI configuration is a direct function of k_{eff} and the temperature difference across the MLI blanket. The use of several different values of k_{eff} is necessary to bound the true heat flow into the tank since an absolute value of k_{eff} at any mean temperature may be highly dependent on the complexity of the MLI system used, the amount of care exercised in the fabrication and attachment of the MLI blanket to the tank, and the number of shields used, as well as the type of spacer material.

The ideal situation would have all heat transfer normal to the MLI blanket by radiation only. The k_{eff} associated with pure thermal radiation between two consecutive shields is given by the following expression:

$$k_{eff} = \frac{\Delta S\ \sigma}{\frac{2}{\epsilon_s} - 1} (T_{k+1} + T_k)\left(T_{k+1}^2 + T_k^2\right)$$

To simulate some conduction between shields, the shield emissivity ϵ_s was arbitrarily multiplied by 10 to a value of 0.24. This curve will be referred to as the k_{eff} of 10 times pure radiation, although the actual increase in heat flow through the MLI blanket

for the same nominal shield spacing and temperature profile was slightly larger.

The k_{eff} associated with pure thermal radiation is compared to the three values of k_{eff} used in this analysis in figure 9. As shown in the figure, a k_{eff} of 10 times pure radiation is very sensitive to temperature, and is below both the k_{eff} of twice the experimental average and that equal to experimental average for temperatures between 40° R (22.2 K) and 218° R (121 K).

The k_{eff} labeled experimental average matches the experimental data of Linde super insulation as stated in reference 9. A mathematical extrapolation of the experimental data, which extended to approximately the temperature of liquid nitrogen, was then made to the temperature of liquid hydrogen. The resulting curve appears to be representative of all existing calorimeter experimental data.

Unpublished experimental data for a continuous-spiral-wrapped cylindrical tank have been superimposed on figure 9. The upper bound represents a 160-shield system, while the lower bound is for a 20-shield system. Clearly, the three curves of k_{eff} chosen for this analysis certainly span the results of this particular experimental program. Furthermore, the manner in which these latter data were taken eliminated the need for questionable mathematical extrapolations to obtain values of k_{eff} at low temperature. The experimental average curve (ref. 9) does not bisect the unpublished experimental data because the data were taken from two completely different sources.

A k_{eff} of twice the experimental average simply multiplies the previous curve by a factor of 2. This curve represents the upper bound in this analysis since it is representative of values obtained on a full-scale tank at mean temperatures of 125° and 225° R (69 and 125 K). The unpublished experimental data indicate that the k_{eff} may be much lower than this curve indicates. However, more data are needed to confirm the actual k_{eff} at low temperatures such as were encountered in this analysis.

An additional uncertainty in the value of k_{eff} that is truly representative of a real situation involves the geometry of the tank and the specific location of the MLI on the tank. The area near the top of the tank, due to the compression of MLI during boost and method of attachment, may have a k_{eff} higher than that at the side of the tank, where the MLI blanket may be allowed to hang straight down. However, the increased thermal performance noted previously for the side of the tank under a 1-g load may be representative of the entire MLI system when subjected to the zero-gravity environment of space.

Optimum Geometric Configuration

Each of the MLI configurations that are discussed in this analysis are shown in cross section. The following items will appear with each figure:

(1) The individual segment heat flows Δq_k across the MLI surface due to radiation exchange as well as Δq_k conducted into the tank for each of the 10 column segments used

(2) The total net heat flow into the tank ΔQ_t, which is the algebraic summation of Δq_k across either of the two surfaces

(3) The size of the segment in angular degrees and number of shields

(4) Various temperatures within the MLI configuration

(5) The location of high-conductivity shields and targeting

(6) The value of k_{eff} used

The base point for all thermal comparisons was the net heat flow into the tank for a constant thickness of 120 shields ($\Delta Q_{t,ct}$) without any high-conductivity shields or targeting. As shown in figure 10, using the k_{eff} of 10 times pure radiation that will be used exclusively in this section of the discussion, $\Delta Q_{t,ct}$ is 1.023 Btu per hour (0.299 J/sec). The following conclusions are clearly indicated in the figure: A severe temperature profile on the MLI surface from the top to the side of the tank does exist. Only the last four segments near the side of the tank show a net rejection of heat to space from their respective surfaces. Selected temperatures within the MLI of the last four segments exceed the corresponding surface temperature of that segment.

Of particular importance is the last statement in the preceding paragraph, describing the temperature inversion within the last four segments. To show this more clearly, the temperature profiles from the MLI surface to the tank wall, for the last five segments at the side of the tank, are shown in figure 11. This effect is attributed to the high lateral-heat-transfer capability of the MLI when compared to the high resistance to heat flow in the normal direction. The result is that the heat rejected at the surface to space requires a substantial temperature gradient to get from the warmer interior of the MLI to the surface.

This is the first indication that a constant-thickness MLI configuration may not be desirable. The constant-thickness MLI configuration sustains a higher temperature within the MLI blanket near the side of the tank than would be achieved with a variable-thickness MLI configuration. This means a high-temperature heat source for further conduction into the tank itself is established. Thus, one of the criteria in obtaining an optimum geometric configuration would be to remove all shields that would lead to a temperature inversion.

Using the same geometric configuration but with a high-conductivity shield at the MLI surface and targeting the last 13° of the MLI surface results in a $\Delta Q_{t,ct}$ of 0.661 Btu per hour (0.194 J/sec), as shown in figure 12. The significant improvement in $\Delta Q_{t,ct}$ is attributed to the interaction of the following effects:

(1) The high-conductivity shield transferred a sufficient quantity of heat laterally to reduce the MLI surface temperatures over the entire surface. This naturally reduced the

temperature profile along the shield adjacent to the tank surface.

(2) Targeting the last segment surface area not only increased the quantity of heat rejected to space but also reduced the steady-state surface temperature at which the heat was rejected. This was a result of $Q/A \simeq \epsilon\sigma T^4$ when the view factor to space approaches 1.

The temperature inversion noted in the preceding configuration also occurred in this configuration. Even though the absolute temperature of the surface was decreased, the relative magnitude of the temperature inversion remained essentially unchanged. The ΔT from the 118th shield to the 88th shield in figure 10 was 48° R (26.7 K) and in figure 12, the ΔT was 49° R (27.2 K).

An initial attempt at customizing the MLI system by removing some MLI and using high-conductivity shields and targeting resulted in the geometric configuration shown in figure 13. The net heat flow into the tank for this customized configuration $\Delta Q_{t,\,cust}$ was 0.302 Btu per hour (0.089 J/sec). The increased thermal performance was attributed to the following chain of events: Varying the MLI thickness (stepping) and using high-thermal-conductivity shields enabled rejection of heat to space from different levels within the MLI configuration. Use of a targeted surface reduced the surface temperature, consequently reducing all MLI interior temperatures below this plane. The optimum configuration would, of course, be that configuration which resulted in temperatures in a plane adjacent to the tank surface near 37° R (20.5 K). This would ensure that the heat flow into the tank would approach zero.

By positioning the high-conductivity shields at different planes within the MLI, a more efficient means of reducing all interior MLI temperatures was achieved. Again because of the high resistance to heat flow in the normal direction, the temperature of a given high-conductivity shield can be reduced more efficiently if the shield is "buried" within the MLI. For the constant-thickness MLI configuration of figure 12, the high-conductivity surface shield was exposed to a constant-temperature heat source when allowed to view the payload directly.

The MLI surface temperatures of those segments near the side of the tank can be further reduced by decreasing the respective view factors of these surfaces to the payload. This was accomplished with the configuration shown in figure 14, where the angular size of the segments near the side of the tank were decreased to 6°. The previous configuration used 13° as the segment size on the last position.

Although decreasing the segment size decreased the surface area of the last segment, it also decreased the geometric radiation view factor of that segment to the payload. With a higher view factor to space, the surface temperature was also reduced. The reduced surface temperature decreased the average temperature in a plane adjacent to the tank from 75° to 59° R (41.7 to 32.8 K). As a result $\Delta Q_{t,\,cust}$ was reduced to 0.107 Btu per hour (0.031 J/sec), or about 10 percent of the base configuration. The physical signifi-

cance of these numbers may be appreciated by noting that similar tankage could tolerate a total (including heat down struts) heat load of 0.7 Btu per hour (0.20 J/sec) when locked up for 1200 days.

The effectiveness of the high-conductivity shields and targeting in reducing $\Delta Q_{t,\,cust}$ was established by rerunning the exact geometric configuration shown in figure 14, except that the high-conductivity shields and targeting were removed. As shown in figure 15, this increased the $\Delta Q_{t,\,cust}$ to 1.01 Btu per hour (0.296 J/sec), a factor of almost 10 higher than that shown in figure 14. Furthermore, the $\Delta Q_{t,\,cust}$ shown in figure 15 is very nearly the same as the thermal performance of the constant-thickness MLI configuration previously discussed in figure 10. Hence, just removing some MLI was not the complete answer to optimizing the MLI configuration. Obviously, the high-conductivity shields and targeting are the major considerations.

The importance of targeting can be readily established when comparing corresponding surface temperatures of untargeted and targeted surfaces, and their resultant effect on the shield temperatures adjacent to the tank. The temperature profiles for the surface shield and shield adjacent to the tank for the configurations shown in figures 14 and 15 are shown in figure 16. The effect of slightly reducing the surface shield temperatures causes a significant decrease in the shield temperature adjacent to the tank. Even the presence of high-conductivity shields that must transfer more heat to the targeted surfaces did not prevent the targeted surface shields from reaching a lower steady-state temperature than the corresponding untargeted shields.

The effectiveness of high-conductivity shields can also be seen in figure 16. For the shield adjacent to the tank, there is a significant ΔT from the top to the side of the tank for the standard shield. However, for the high-conductivity shield, this temperature difference appears to be negligible.

The customized MLI configuration shown in figure 17, yielding a $\Delta Q_{t,\,cust}$ of 0.019 Btu per hour (0.006 J/sec), was obtained

(1) By decreasing the angular size of the segments near the side of the tank to 4°

(2) By increasing the number of shields over the angular segments near the side of the tank, but staying below the point where a temperature inversion might occur

(3) By targeting those surfaces near the side of the tank where the temperature and view factor to space permit a net rejection of heat to space

(4) By using high-conductivity shields in any plane where targeting is also used

Since further perturbations in this geometry resulted in insignificant changes in $\Delta Q_{t,\,cust}$, this geometry was considered to be the optimum. The $\Delta Q_{t,\,cust}$ for this optimum configuration was less than 2 percent of that obtained with the constant-thickness MLI configuration, without targeting or high-conductivity shields, as shown in figure 10.

Thermal Effectiveness for Various Values of k_{eff}

The net heat flows into the tank for a constant-thickness MLI configuration $\Delta Q_{t,ct}$ are compared to the net heat flows into the tank for the optimum customized configuration $\Delta Q_{t,cust}$ in table I for the three different values of k_{eff} used in this analysis. The thermal performance of the constant-thickness MLI configuration was obtained with and without the use of high-conductivity shields and targeting.

As stated previously, the constant-thickness MLI configuration arbitrarily used 120 shields as the base point of comparison. In order to make the comparisions compatible, the customized configurations also used a maximum of 120 shields at any location on the tank. The arbitrary selection of 120 shields was made only to evaluate the concepts proposed in this analysis. For an actual application, increased thermal protection may be obtained by increasing the number of shields.

The thermal effectiveness η of any configuration was arbitrarily defined as the ratio of $\Delta Q_{t,ct}$ without targeting or high-conductivity shields to $\Delta Q_{t,cust}$ for the optimum customized configuration. The results of the previous section for the MLI configurations shown in figures 10, 12, and 17 are listed in table I for a k_{eff} of 10 times pure radiation. Thus, η for the constant thickness with targeting and a high-conductivity shield is 1.55, while η for the optimum customized configuration is 53.84.

The constant-thickness configuration of figure 10 was rerun using a k_{eff} representing an experimental average value. For this configuration, shown in figure 18 without high-conductivity shields or targeting, $\Delta Q_{t,ct}$ was 1.185 Btu per hour (0.347 J/sec). The thermal performance of the same configuration but with a high-conductivity shield at the surface and targeting is 0.903 Btu per hour (0.265 J/sec), as shown in figure 19.

Since k_{eff} against temperature for the experimental average value is much more linear than that for a k_{eff} of 10 times pure radiation, the resulting temperature profile through the MLI is also more linear. This results in a substantially lower temperature profile on the shield adjacent to the tank, even though the net heat flows into the tank are approximately the same.

The fact that the resulting temperature inversion using the experimental average value for k_{eff} is much less severe can be attributed to the following effects: The lateral heat-transfer capability of the MLI remains essentially the same, while the temperature gradient in the normal direction can be less steep for the higher k_{eff} to transfer the same quantity of heat. However, it is again readily seen that the constant-thickness MLI may actually reduce the thermal performance, for the same reasons stated previously.

The same geometry of the optimized configuration determined in the preceding section of the discussion (fig. 17) was also rerun using the experimental value of k_{eff}, except that additional layers of MLI were added to the segments near the side of the tank. This was possible since the more linear temperature profile through the MLI enabled

more MLI to be applied before a temperature inversion occurred.

Several MLI configurations were evaluated to verify that this particular geometry represented an optimum. The optimum configuration was established when additional perturbations in the geometry did not significantly change the value of $\Delta Q_{t,\,cust}$ of 0.231 Btu per hour (0.068 J/sec) shown in figure 20. The minor improvement in thermal performance achieved by adding more layers of MLI at the side of the tank must be done at the expense of increased MLI weight. The weight of added MLI must be balanced against the reduction of the weight of propellant lost to boiloff, or a reduction in the system weight associated with bulk heating.

The much less substantial thermal effectiveness η of 5.13 obtained using a k_{eff} of experimental average can be attributed to the increased value of k_{eff} at the low temperatures acting over the same differential temperature. This differential temperature is the MLI surface temperature of the last segment minus the tank wall temperature. Using a high-conductivity shield in this position ensures that this temperature is approximately constant in this plane. As will be shown later, this steady-state surface temperature is fixed by the radiation view factor to space, and is relatively independent of the k_{eff} of the MLI blanket.

The identical MLI configurations shown in figures 18 to 20 were rerun using a k_{eff} representing a value of twice the experimental average. The results are shown in figures 21 to 23 and are listed in table I. The value of η obtained for the optimum customized configuration was 3.44.

The MLI surface temperature profiles from the constant-thickness MLI configurations shown in figures 10, 12, 18, 19, 21, and 22 are compared in figure 24. For the case of no targeting or high-conductivity shield at the surface, the temperature profile on the MLI surface is relatively independent of the k_{eff} of the MLI blanket. The same conclusion is valid for the other case of targeting and use of a high-conductivity shield at the surface. This would seem to substantiate the conclusion that the steady-state MLI surface temperature established is a function basically of the geometric radiation view factor to the payload and the surface emissivity, and not influenced by the MLI performance.

Further indication that targeting the MLI surface reduces the steady-state surface temperature can also be seen in figure 24. Once again, the clear-cut advantage of targeting as a technique of increasing thermal performance can be noted. Decreasing the surface temperature of a constant-thickness MLI blanket obviously has to decrease the heat flow through the MLI blanket.

Effect of Changes in Program Variables on Thermal Performance

All attempts to further improve the thermal performance of the optimized MLI con-

figuration by decreasing the angular size of the segments used at the side of the tank were unsuccessful. One configuration using 2° as the size of the last segment resulted in violent oscillations in the surface temperature of this segment between consecutive iterations. This meant the program was not able to converge asymptotically to a steady-state temperature.

The inability of the program to iterate to a stable surface temperature is attributed to the large change in the physical constants used to define this configuration. As the segment size was decreased, the view factor to the payload was significantly decreased. This would tend to establish a low steady-state surface temperature. However, the decreased surface area of the segment was unable to reject the increased lateral heat transfer to that segment resulting from the lower temperature. Hence, the program would "guess" a much higher temperature for the next iteration. Thus although the equations used to describe the physical problem remained correct, the solution of these equations became mathematically unstable.

It appears that the 4° angle of the last segment approaches the optimum. This is substantiated by the configuration shown in figure 25, in which the area of the last segment has been doubled. In this configuration, the additional area is the mirror image of the 10th segment, and is located just below the equator of the tank. The increased area for heat rejection plus the effect of this area "seeing" only space would seem sufficient cause to lower the effective surface temperature substantially and thus increase the thermal performance significantly. However, this is not the case. The surface temperature goes from 94° R (52.2 K) for the comparable configuration shown in figure 23 to only 84° R (46.7 K) for this configuration. The corresponding $\Delta Q_{t,\,cust}$ is decreased from 0.647 Btu per hour (0.190 J/sec) to 0.535 Btu per hour (0.157 J/sec). Apparently, two conflicting trends limit the degree of thermal performance obtained. As the surface temperature decreases, the lateral heat flow increases; however, the quantity of heat rejected is decreased.

The thermal performances of the optimum customized configuration using a payload emissivity of 0.024 instead of 0.11 and a k_{eff} of the experimental average and of twice the experimental average are shown in figures 26 and 27 and are also tabulated in table I. The values of $\Delta Q_{t,\,cust}$ for both values of k_{eff} used were each reduced to 47 percent of the respective values obtained with an emissivity of 0.11. The increase in thermal performance obtained by decreasing the payload emissivity from 0.11 to 0.024 is directly attributed to the reduced MLI surface temperatures, which caused a reduced temperature profile in a plane adjacent to the tank. The decreased surface temperatures result from decreasing the energy incident on the surface by reducing the payload emissivity.

The optimum configuration of figure 23 was rerun with the surface emissivities changed from an untargeted value of 0.024 to 0.015 and a targeted value of 0.9 to 0.75. The approximately 3 percent change in ΔQ_t for this configuration shown in figure 28

when compared to figure 23 was considered to be negligible in view of the significant change in the emissivities.

The configurations shown in figures 17 and 23 were rerun with the tank-payload spacing doubled. As shown in figure 29 for a k_{eff} of 10 times pure radiation, ΔQ_t was 68 percent of the value shown in figure 17. Using a k_{eff} of twice the experimental average, the ΔQ_t shown in figure 30 was 86 percent of the value listed in figure 23. The MLI surface temperatures at the top of the tank are changed more significantly than those temperatures at the side of the tank. This occurred because the geometric radiation view factor changes more significantly near the top of the tank as the tank-payload spacing is doubled.

Multilayer Insulation System Weights

A dimensionless parameter W_{MLI} representing the ratio of the weight of the optimum customized MLI system to the weight of a constant thickness of MLI was determined for each of the three values of k_{eff} used in this analysis. This ratio expressed the relative weights (rather than absolute weights) by summing the products of the number of shields times the surface area covered for all 10 tank segments. The results as listed in table I are as follows: $W_{MLI} = 0.706$ for k_{eff} equal to 10 times pure radiation and 0.822 for k_{eff} equal to the experimental average as well as for k_{eff} equal to twice the experimental average. The ratio is the same for the last two values of k_{eff} since the same configuration was used for both.

Thus, in addition to increasing the thermal performance, the customized concept also reduces the total weight of the MLI required. A reduction of the quantity of MLI required may also make fabrication and installation of the MLI blanket much less difficult.

CONCLUDING REMARKS

An analytical investigation was conducted to determine the space-hold thermal performance of MLI on the upper half of an unshrouded liquid hydrogen tank within a sun-oriented vehicle. The thermal model used the geometry of a $\sqrt{2}$ oblate spheroidal tank having a major diameter of 9.142 feet (2.786 m). The tank was assumed to be in the shadow of a 10-foot- (3.048-m-) diameter flat-surfaced payload maintained at a constant temperature of 520° R (289 K).

The analysis showed that the space-hold thermal performance of a given thickness of

conventional MLI on the top half of the liquid hydrogen tank can be significantly improved

1. By varying the MLI thickness from a maximum at the top of the tank to a minimum at the side of the tank, where the radiation view factor to space is a maximum: As established in this analysis, the constant-thickness MLI configuration degrades thermal performance since it sustains a higher temperature within the MLI blanket near the side of the tank than would be achieved with a variable-thickness MLI configuration.

2. By increasing the surface emissivity (targeting) of the shields in the area where the view factor to space is highest: The thermal improvement occurred since targeting not only increased the quantity of heat rejected to space, but also reduced the steady-state surface temperature at which the heat was rejected.

3. By using high lateral-thermal-conductivity shields within the MLI that become the top shield of consecutive segments of different MLI thicknesses at the side of the tank: By positioning the high-conductivity shields at different planes within the MLI, a more efficient means of reducing all interior MLI temperatures was achieved.

The analysis showed that simply varying the MLI thickness alone did not change the thermal performance appreciably. The optimum customized configuration required a combination of these three changes. Optimum is defined as that particular geometry for which further perturbations did not significantly change the thermal performance.

The net heat flows into the tank through the optimum customized configuration were determined for three different values of effective normal thermal conductivity k_{eff}. The net heat flows were 0.019, 0.231, and 0.647 Btu per hour (0.006, 0.068, and 0.190 J/sec), respectively, for k_{eff} of 10 times pure radiation, the experimental average, and twice the experimental average. These heat flows were a factor of 53.84, 5.13, and 3.44 lower than the corresponding net heat flows for the conventional constant-thickness MLI configurations. The degree of improvement realized was very sensitive to the value of k_{eff} at low mean temperatures.

As shown in this investigation, the steady-state MLI surface temperature established for any MLI surface segment was highly dependent on the geometric radiation view factor between that surface segment and the payload, as well as the emissivity used for that particular surface segment. The value of k_{eff} used for the MLI blanket had little effect on what this steady-state surface temperature should be. Thus, for a fixed MLI thickness and approximately the same boundary temperatures, the net heat flow into the tank is dependent solely on k_{eff}.

The optimum configuration used angular segments of 4° for each of the last three tank segments regardless of the effective normal conductivity used. This was the result of a trade-off between decreasing this angle to give a higher radiation view factor to space (lower steady-state surface temperature) while still trying to reject a certain quantity of heat from a smaller area at a lower temperature. Doubling the surface area of the last

segment by adding the mirror image of this area from the bottom half of the tank did not result in a significant increase in thermal performance.

Using a payload emissivity of 0.024 instead of 0.11 reduced the net heat flow into the tank to 47 percent of the original value. These results were obtained with the optimum customized configuration for a k_{eff} of experimental average as well as for a k_{eff} of twice the experimental average.

Doubling the tank-payload spacing decreased the net heat flow into the tank by 32 percent for a k_{eff} of 10 times pure radiation. For a k_{eff} of twice experimental average, the corresponding decrease was only 14 percent.

In addition to the increased thermal performance, the weight of the optimum customized MLI system was approximately 0.706 times the weight of a constant-thickness MLI system when using a k_{eff} of 10 times radiation. The optimum customized MLI systems for the other two values of k_{eff} were identical. The use of additional shields near the side of the tank resulted in a weight ratio of 0.822.

Lewis Research Center,
National Aeronautics and Space Administration,
Cleveland, Ohio, November 3, 1970,
180-31.

APPENDIX - SYMBOLS

A	area, ft^2; m^2
ΔA, dA	incremental area, ft^2; m^2
$A_i F_{i,j}$	product of area of ith surface times geometric radiation view factor between i^{th} and j^{th} surfaces, ft^2; m^2
$F_{i,j}$	geometric radiation view factor, portion of total energy, either emitted or reflected diffusely from surface i, that is intercepted by surface j
h	tank-payload spacing, ft; m
k	thermal conductivity, Btu/(hr)(ft)(^oR); J/(sec)(m)(K)
k_{eff}	effective thermal conductivity normal to MLI blanket, Btu/(hr)(ft)(^oR); J/(sec)(m)(K)
L	length, ft; m
N	number of surfaces in enclosure
n	number of shields per cell
Q	heat flow, Btu/hr; J/sec
ΔQ_t	total net heat flow through MLI blanket and into tank, Btu/hr; J/sec
q	incremental heat flows, either across a plane of any segment or into (or out of) any surface segment, Btu/hr; J/sec
Δq	net heat flow into any given segment, Btu/hr; J/sec
R	distance between any two incremental surfaces, ft; m
ΔS	shield spacing, in.; cm
T	temperature, ^oR; K
ΔT	temperature difference, ^oR; K
V	volume, ft^3; m^3
W_{MLI}	ratio of weight of optimum customized MLI system to weight of constant-thickness MLI system
w	thickness or width, in.; cm
ϵ	emissivity
η	effectiveness, $\Delta Q_{t,ct}/\Delta Q_{t,cust}$
σ	Stefan-Boltzmann constant, 0.173×10^{-8} Btu/(ft^2)(hr)($^oR^4$); 5.67×10^{-8} J/(m^2)(sec)(K^4)
φ	angle between normal to surface and vector R from that surface

Subscripts:

al	aluminum
arc	circle segment
ct	constant thickness
cust	customized
hc	high-conductivity cell
in	incoming
i, j, k, l	surface index or counter
lat	lateral
m, n	reference or index
norm	normal
out	outgoing
p	payload

r	rejected	t	tank
s	shield	1	tank surface increment
sc	standard cell	2	payload surface increment
surf	surface		

REFERENCES

1. Johnson, William R.; and Sprague, Earl L.: Analytical Investigation of Thermal Degradation of High-Performance Multilayer Insulation in the Vicinity of a Penetration. NASA TN D-4778, 1968.
2. Cowgill, Glenn R.; and Johnson, William R.: Computer Program for Thermal Analysis of Tank Mounted Multilayer Insulation. NASA TN D-6228, 1971.
3. Eckert, E. R. G.; and Drake, Robert M., Jr.: Heat and Mass Transfer. Second ed., McGraw-Hill Book Co., Inc., 1959.
4. Cunnington, G. R.; and Tien, C. L.: A Study of Heat-Transfer Processes in Multilayer Insulations. Paper 69-607, AIAA, June 1969.
5. Knoll, Richard H.; and Bartoo, Edward R.: Experimental Studies on Shadow Shields for Thermal Protection of Cryogenic Tanks in Space. NASA TN D-4887, 1968.
6. Anon.: Advanced Studies on Multi-Layer Insulation Systems. Rep. ADL-67180-00-04, Arthur D. Little, Inc. (NASA CR-54929), June 1, 1966.
7. Hall, W. M.: Effect of Low Temperature on the Thermal Emittance of Three Black Paints; Comparison of Normal and Hemispherical Emittances. Space Programs Summary No. 37-31, Vol. IV, Jet Propulsion Lab., California Inst. Tech. (NASA CR-62607), Feb. 28, 1965, pp. 108-109.
8. Coston, R. M.: Handbook of Thermal Design Data for Multilayer Insulation Systems, Vol. II. Rep. LMSC-A847882, Vol. II, Lockheed Missiles and Space Co. (NASA CR-87485), June 25, 1967.
9. Olivier, J. R.; and Dempster, W. E.: Orbital Storage of Liquid Hydrogen. NASA TN D-559, 1961.

TABLE I. - COMPARISON OF MULTILAYER INSULATION THERMAL PERFORMANCES OF PRIMARY IMPORTANCE

Configuration[a]	Figure	Normal thermal conductivity, k_{eff}	Payload emissivity, ϵ_p	Tank-payload spacing, h		Net heat flow, ΔQ_t		Thermal effectiveness, η	MLI weight ratio, W_{MLI}
				ft	m	Btu/hr	J/sec		
A	10	Ten times pure radiation	0.11	0.8175	0.2492	1.023	0.299	1.00	1.000
B	12		↓	.8175	.2492	.661	.194	1.55	1.010
C	17			.8175	.2492	.019	.006	53.84	.706
C	29			1.6350	.4984	.013	.004	78.69	.706
A	18	Experimental average	0.11	0.8175	0.2492	1.185	0.347	1.00	1.000
B	19		.11	↓	↓	.903	.265	1.31	1.010
C	20		.11			.231	.068	5.13	.822
C	26		.024			.109	.032	10.87	.822
A	21	Twice the experimental average	0.11	0.8175	0.2492	2.226	0.652	1.00	1.000
B	22		.11	↓	↓	1.714	.502	1.30	1.010
C	23		.11			.647	.190	3.44	.822
C	27		.024			.306	.090	7.27	↓
C'	28		.11			.667	.196	3.34	
C	30		.11	1.6350	.4984	.558	.163	3.99	

[a]A - Constant MLI thickness (120 shields), no targeting or high-conductivity shields.

B - Constant MLI thickness (120 shields), with targeting and high-conductivity shield at surface.

C - Optimum customized MLI configuration.

C' - Optimum customized MLI configuration, except $\epsilon_{targeted} = 0.75$ and $\epsilon_{untargeted} = 0.015$.

All other configurations: $\epsilon_{targeted} = 0.9$, $\epsilon_{untargeted} = 0.024$.

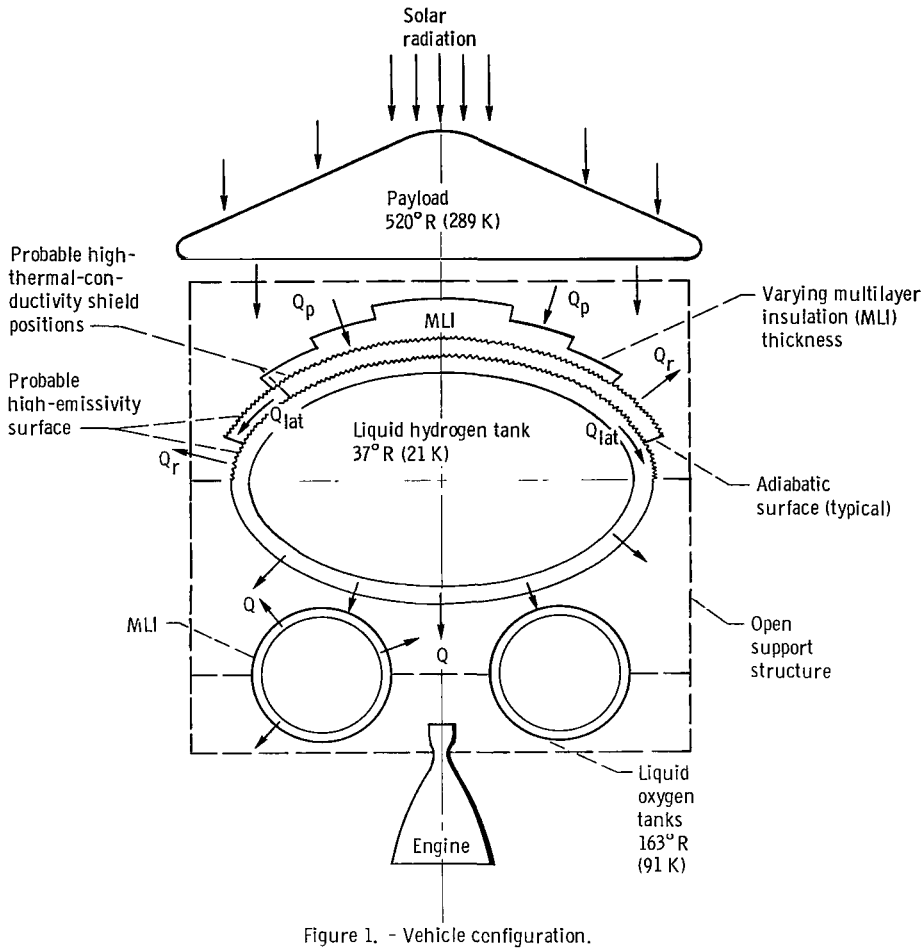

Figure 1. - Vehicle configuration.

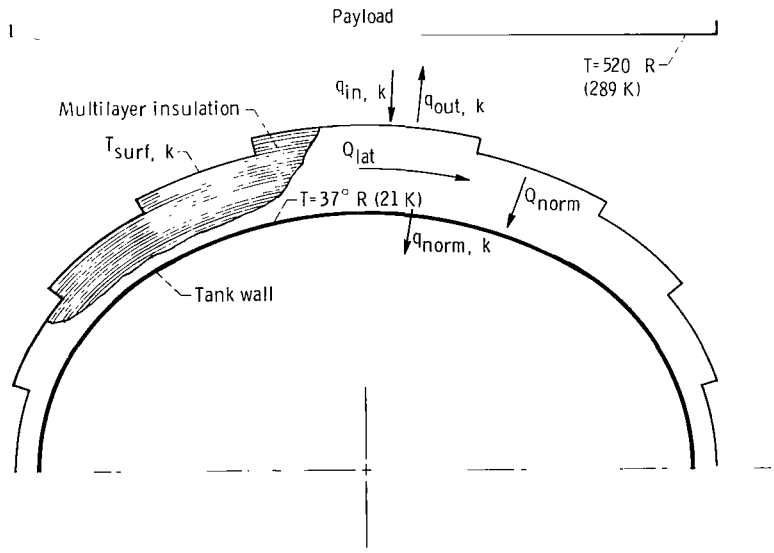

Figure 2. - Cross-sectional view of model.

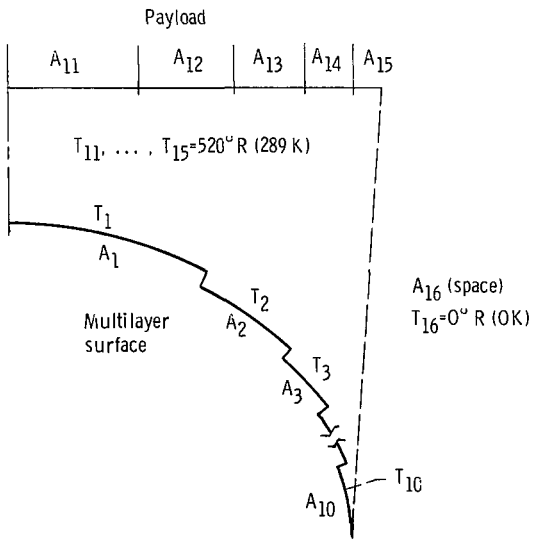

Figure 3. - Enclosure for radiation exchange.

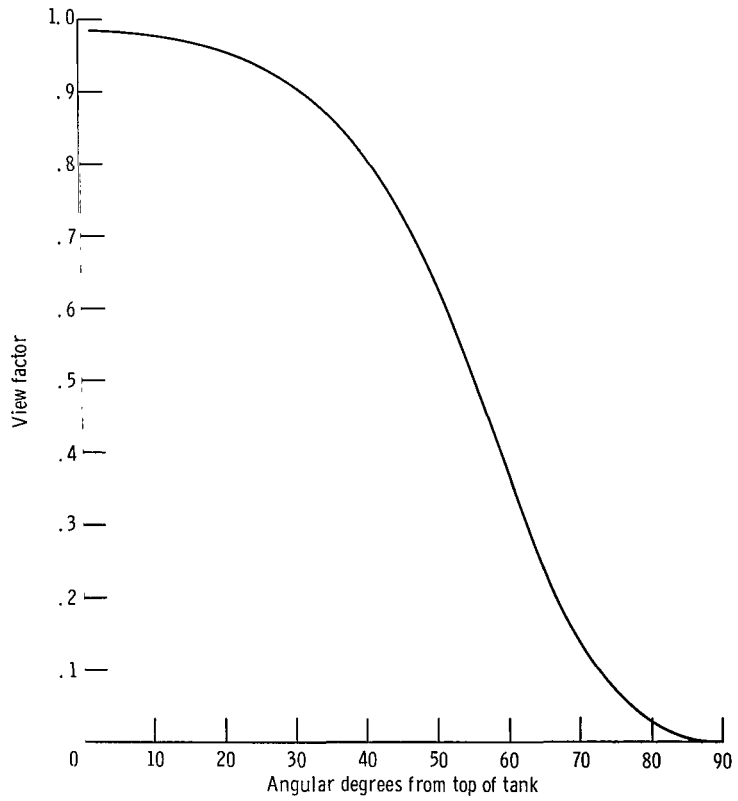

Figure 4. - Geometric radiation view factor between tank surface and payload as function of angular position from top of tank. Typical for constant multilayer insulation (MLI) thickness of 120 shields and a tank-payload spacing of 0.8175 foot (0.2492 m).

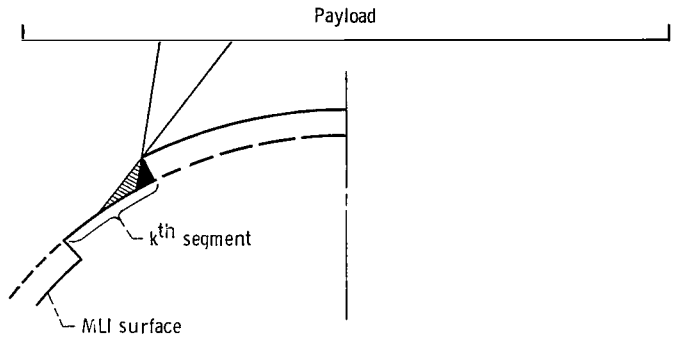

Figure 5. - Shadow effect on view factor for variable-thickness multilayer insulation (MLI) configuration.

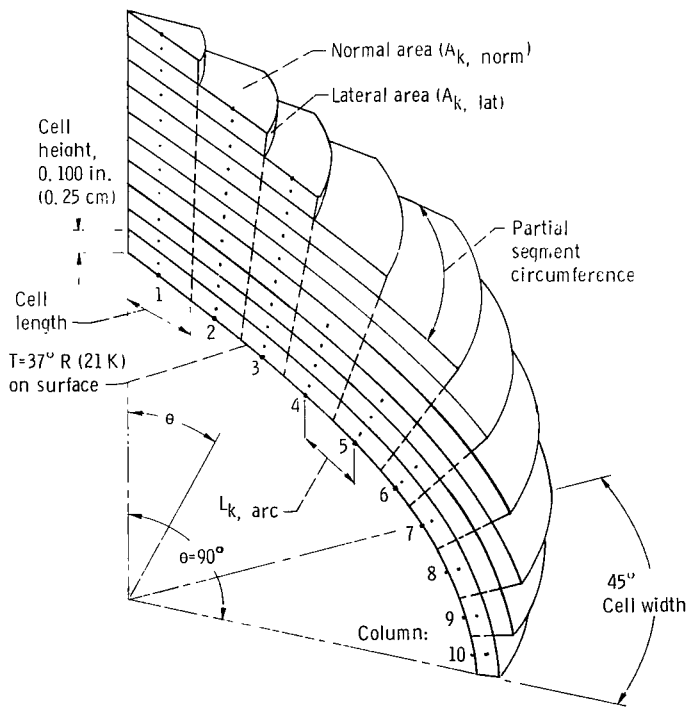

Figure 6. - 45° Segment of multilayer insulation divided into cells.

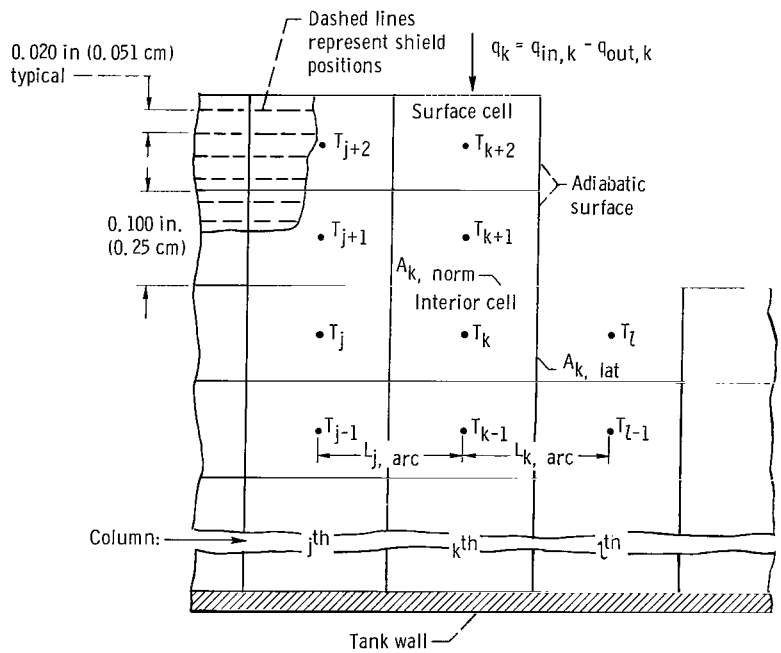

Figure 7. - Cross-sectional view of several cells.

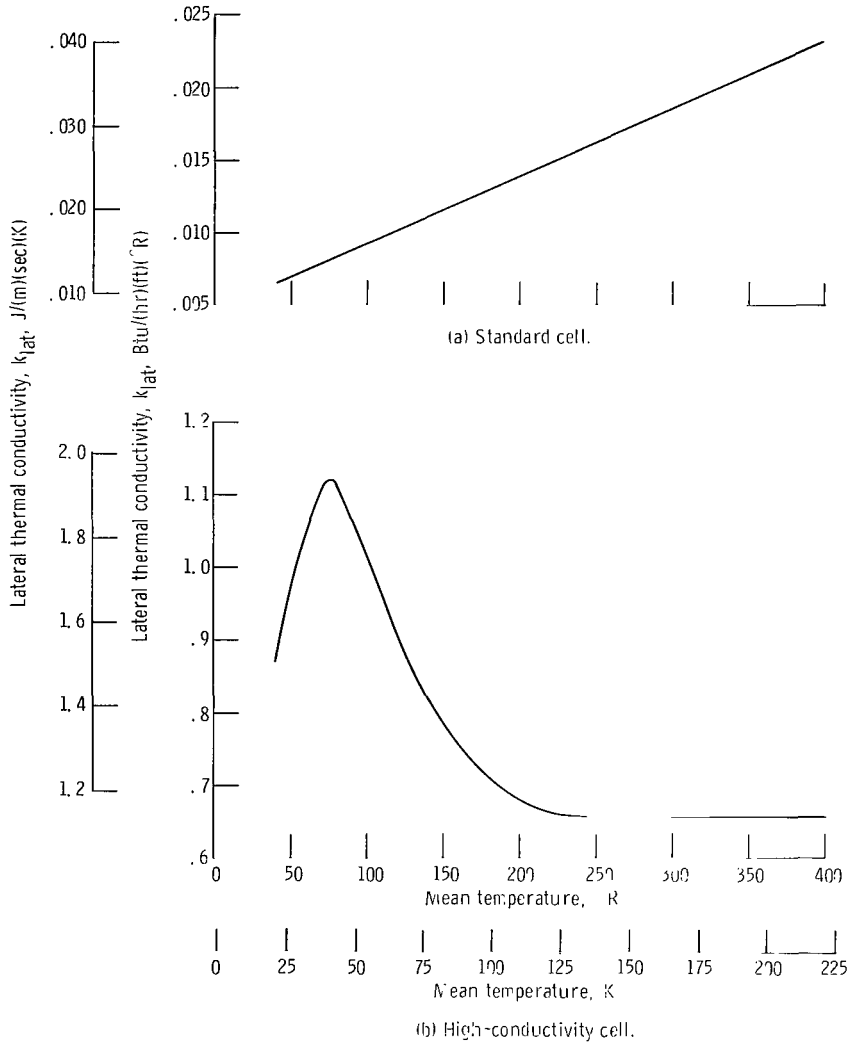

Figure 8. - Lateral thermal conductivity of multilayer insulation cells against temperature. (Data from ref. 8.)

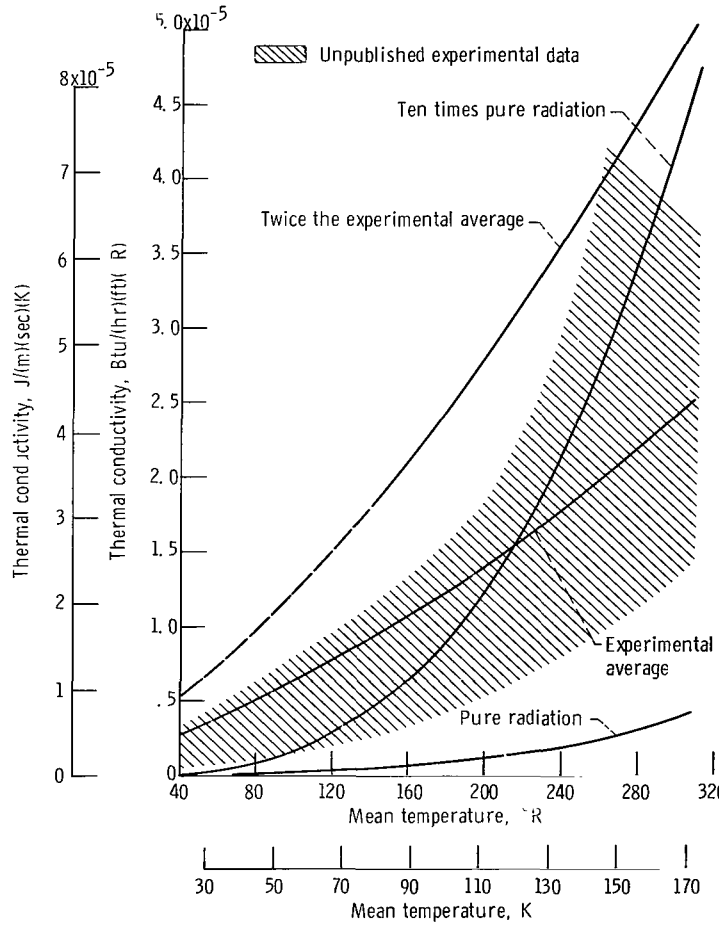

Figure 9. - Effective thermal conductivity normal to multilayer insulation as function of temperature.

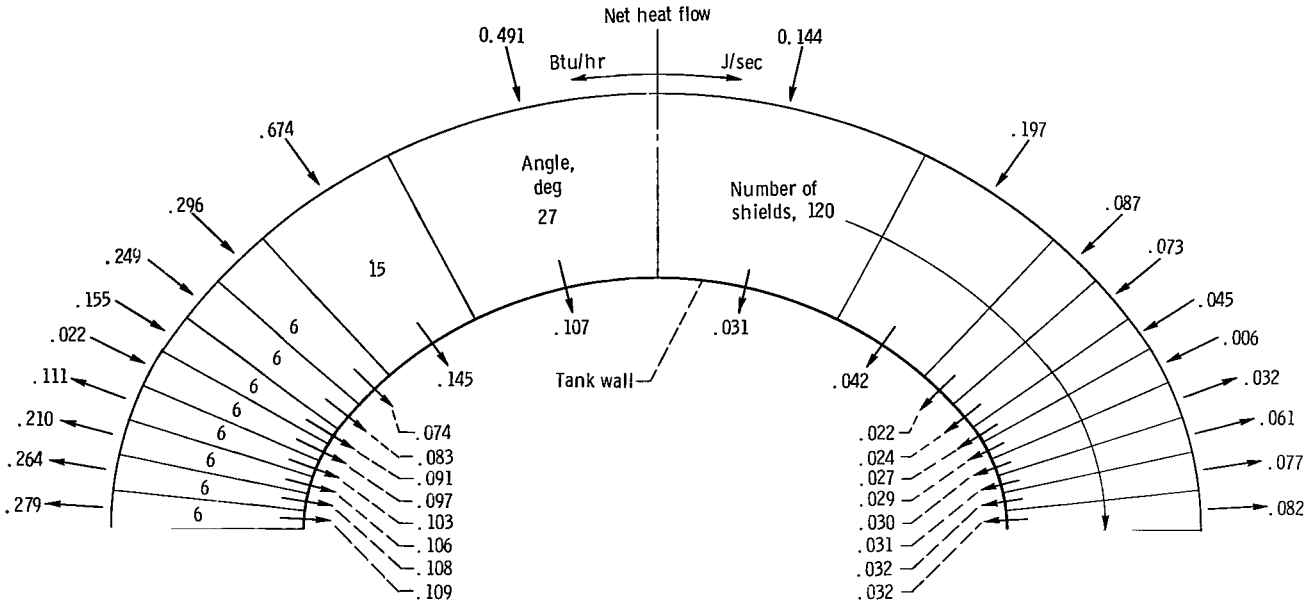

(a) Net heat flows across segment boundaries; total net heat flow, 1.023 Btu per hour (0.299 J/sec).

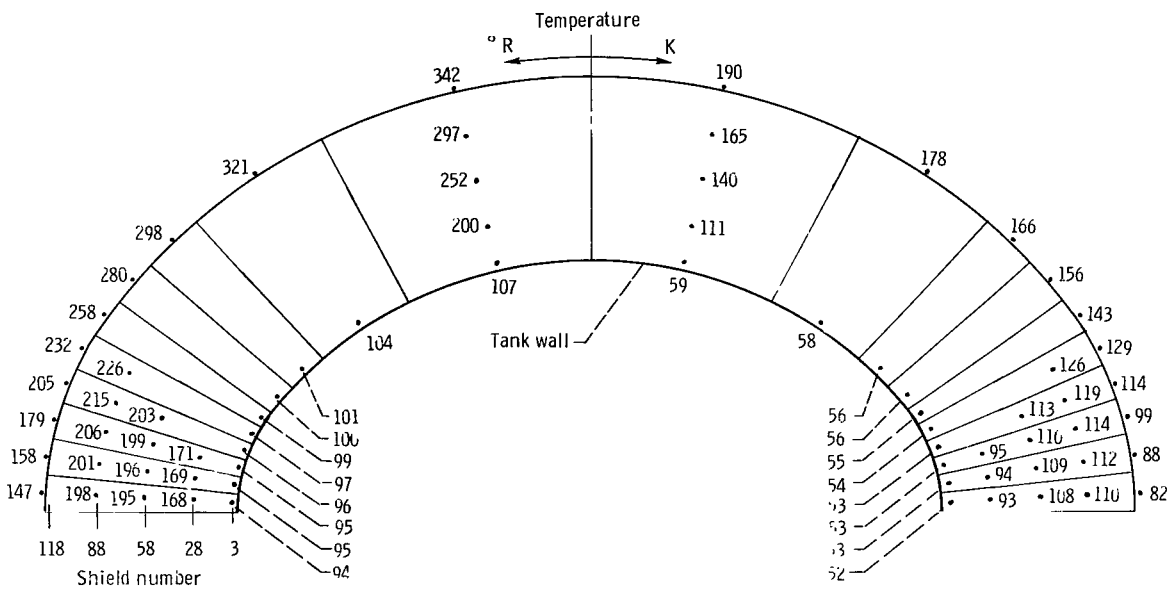

(b) Temperature distribution.

Figure 10. - Results of analysis for constant multilayer insulation thickness using effective normal thermal conductivity of 10 times pure radiation. No high-lateral-thermal-conductivity shields or targeting; untargeted multilayer insulation surface emissivity, 0.024; payload emissivity, 0.11.

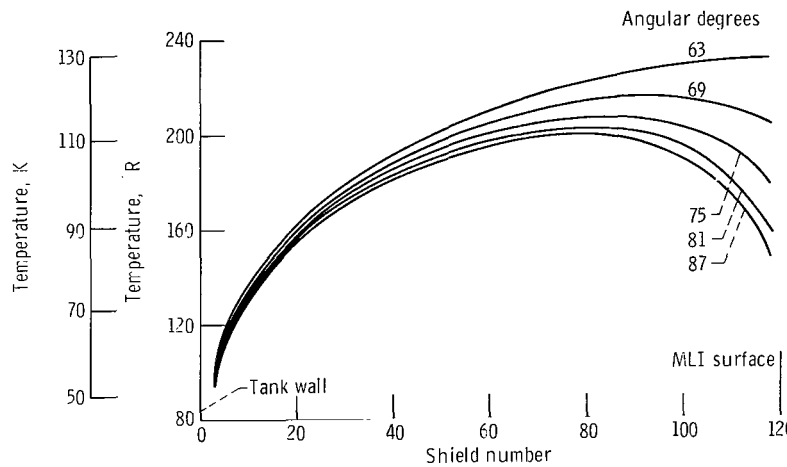

Figure 11. - Temperature inversion through multilayer insulation (MLI), typical of constant MLI thickness, as function of angular location from top of tank. (Data from fig. 10.)

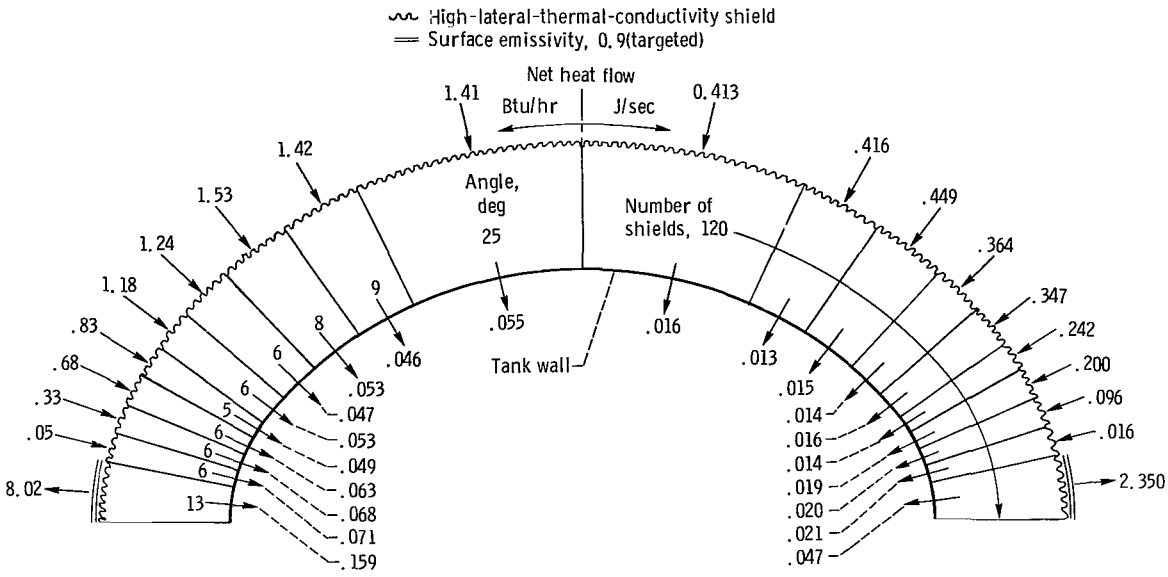

(a) Net heat flows across segment boundaries; total net heat flow, 0.661 Btu per hour (0.194 J/sec).

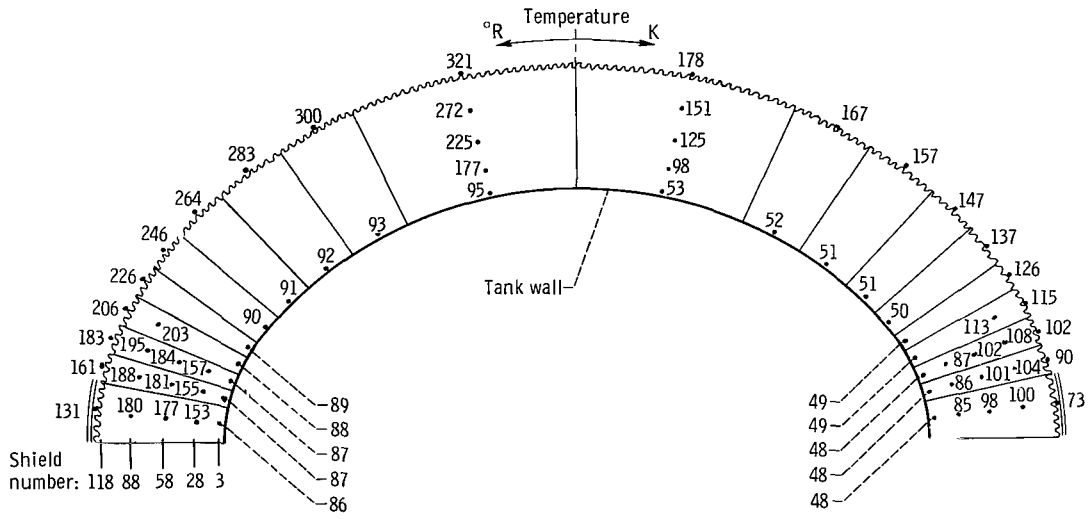

(b) Temperature distribution.

Figure 12. - Results of analysis for constant multilayer insulation (MLI) thickness using effective normal thermal conductivity of 10 times pure radiation. High-lateral-thermal-conductivity shield at surface and targeting last segment surface; untargeted MLI surface emissivity, 0.024; payload emissivity, 0.11.

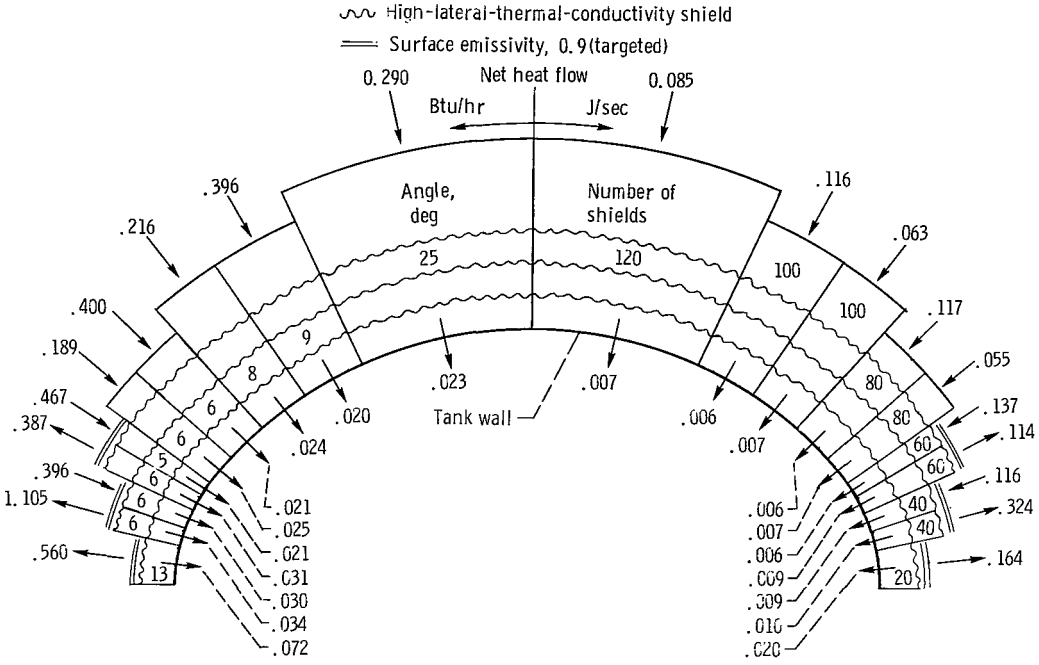

(a) Net heat flows across segment boundaries; total net heat flow, 0.302 Btu per hour (0.089 J/sec).

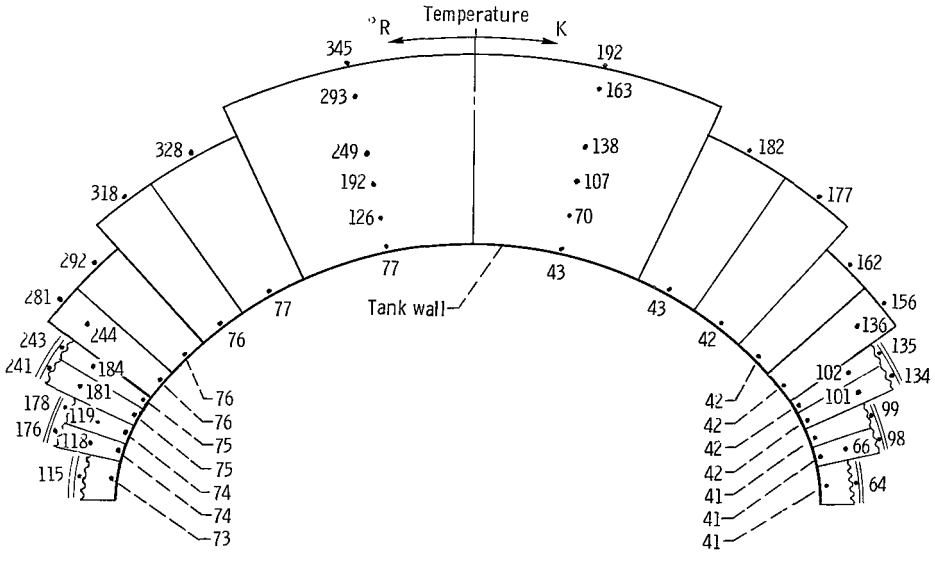

(b) Temperature distribution.

Figure 13. - Results of analysis for variable multilayer insulation (MLI) thickness using effective normal thermal conductivity of 10 times pure radiation; three high-lateral-thermal-conductivity shields and three surface segments targeted. Untargeted MLI surface emissivity, 0.024; payload emissivity, 0.11.

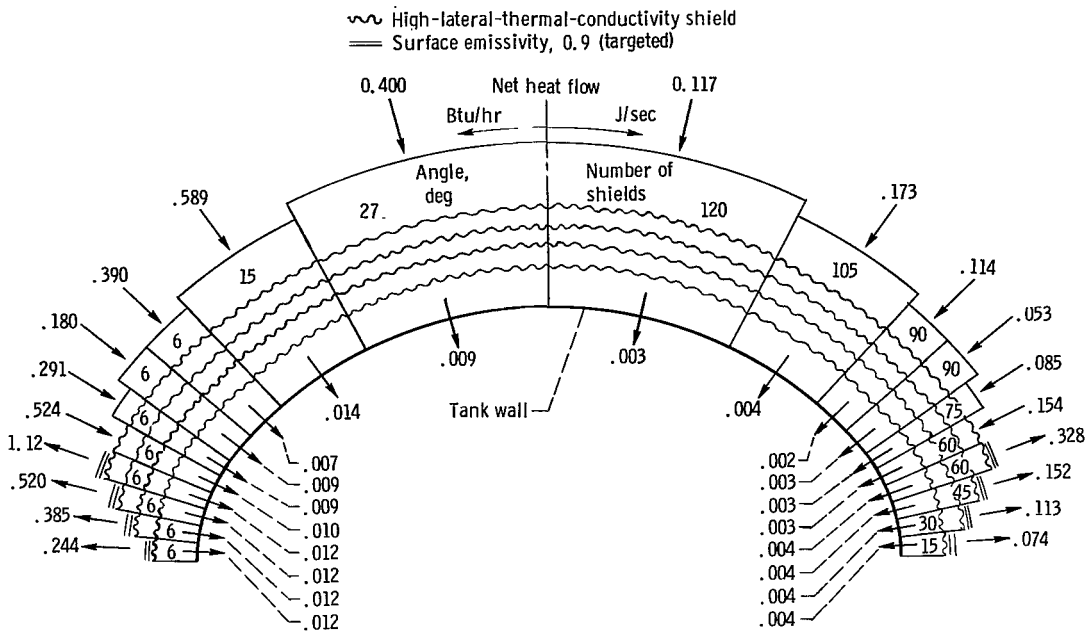

(a) Net heat flows across segment boundaries; total net heat flow, 0.107 Btu per hour (0.031 J/sec).

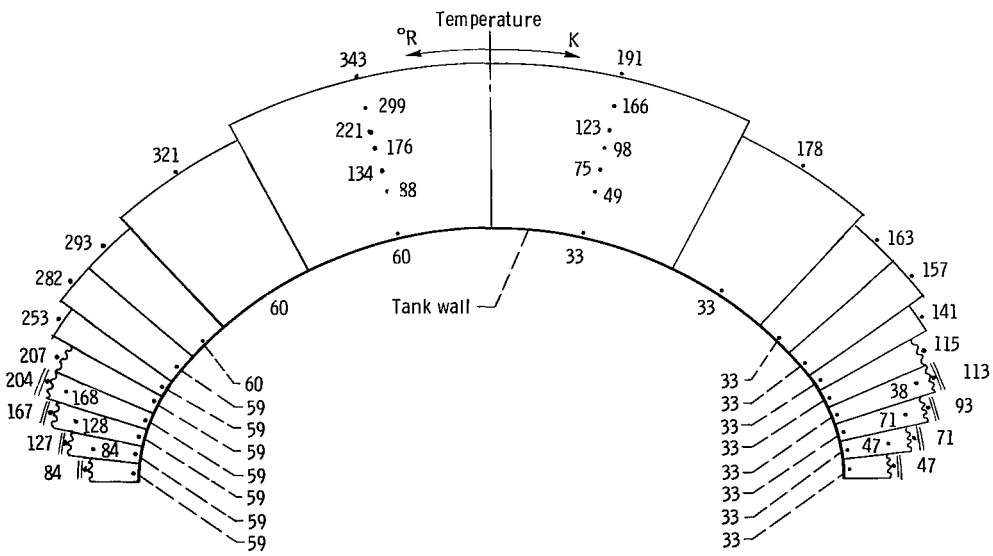

(b) Temperature distribution.

Figure 14. - Results of analysis for variable multilayer insulation (MLI) thickness using effective normal thermal conductivity of 10 times pure radiation; four high-lateral-thermal-conductivity shields and four surface segments targeted. Untargeted MLI surface emissivity, 0.024; payload emissivity, 0.11.

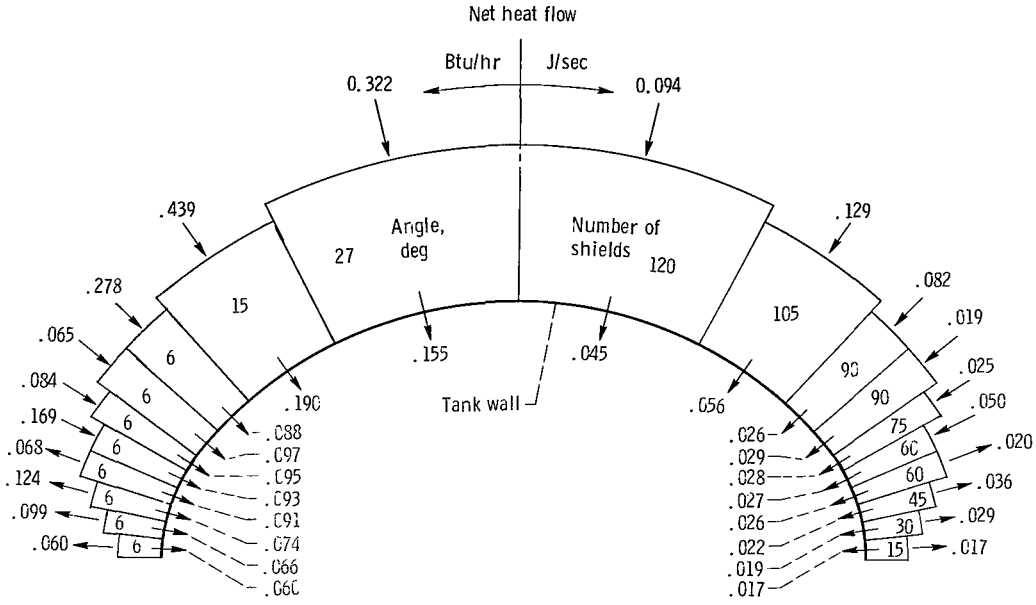

(a) Net heat flows across segment boundaries; total net heat flow, 1.01 Btu per hour (0.296 J/sec).

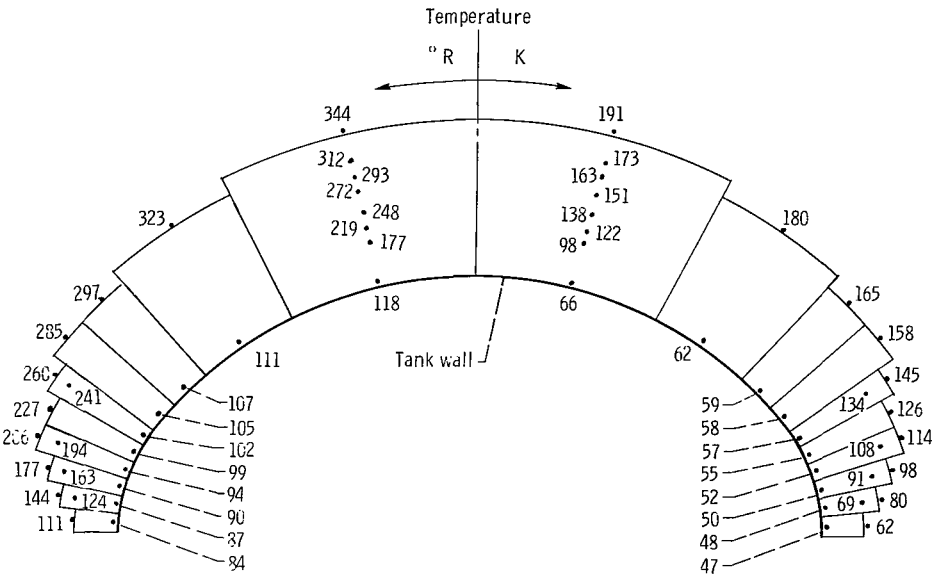

(b) Temperature distribution.

Figure 15. - Results of analysis for multilayer insulation (MLI) configuration shown in figure 14 with high-lateral-thermal-conductivity shields and targeting both removed.

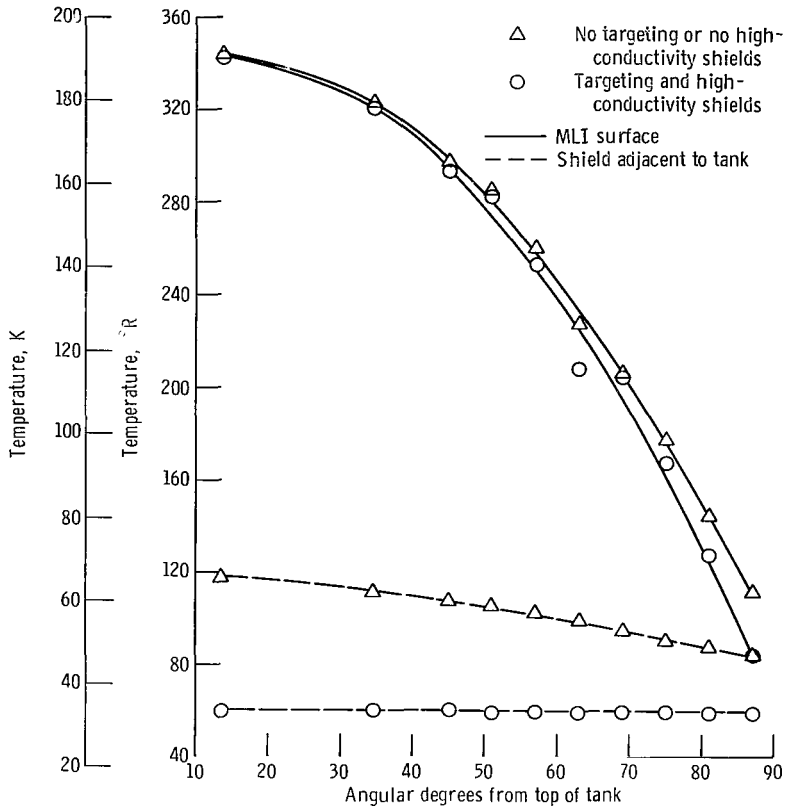

Figure 16. - Temperature profiles for same geometric multilayer insulation (MLI) configuration with and without use of targeting and high-conductivity shields. (Data from figs. 14 and 15.)

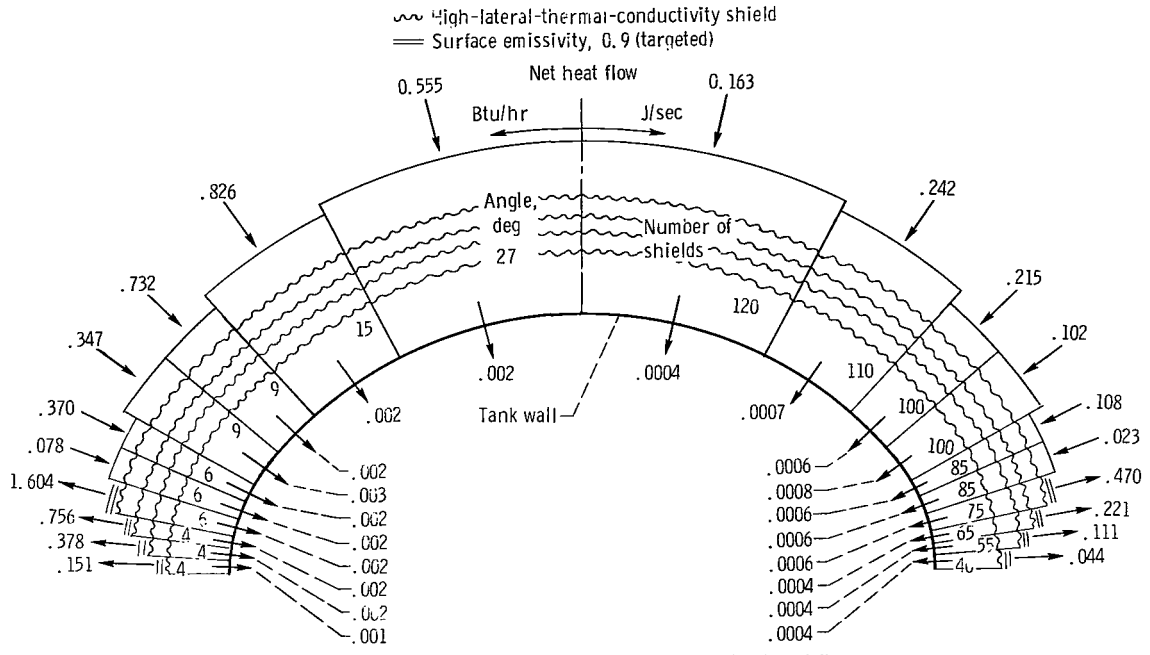

(a) Net heat flows across segment boundaries; total net heat flow, 0.019 Btu per hour (0.006 J/sec).

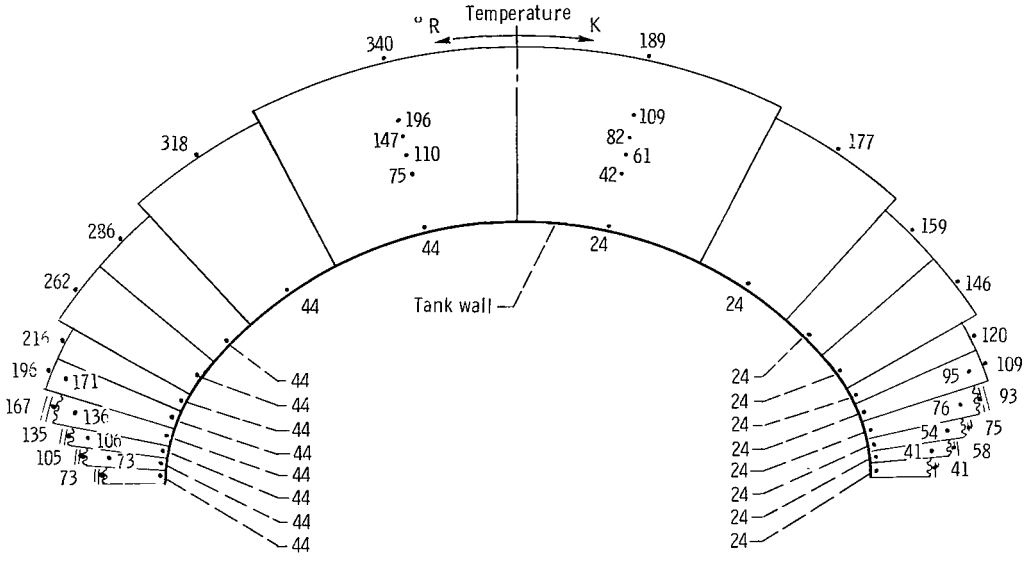

(b) Temperature distribution.

Figure 17. - Results of analysis for optimum customized multilayer insulation (MLI) configuration using effective normal thermal conductivity of 10 times pure radiation. Untargeted MLI surface emissivity, 0.024; payload emissivity, 0.11.

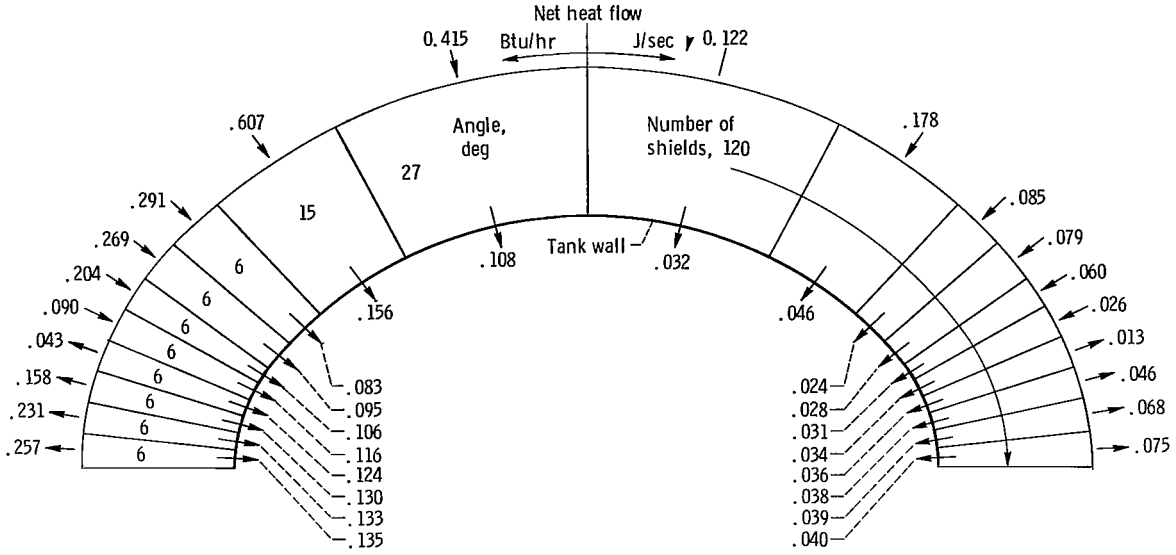

(a) Net heat flows across segment boundaries; total net heat flow, 1.185 Btu per hour (0.347 J/sec).

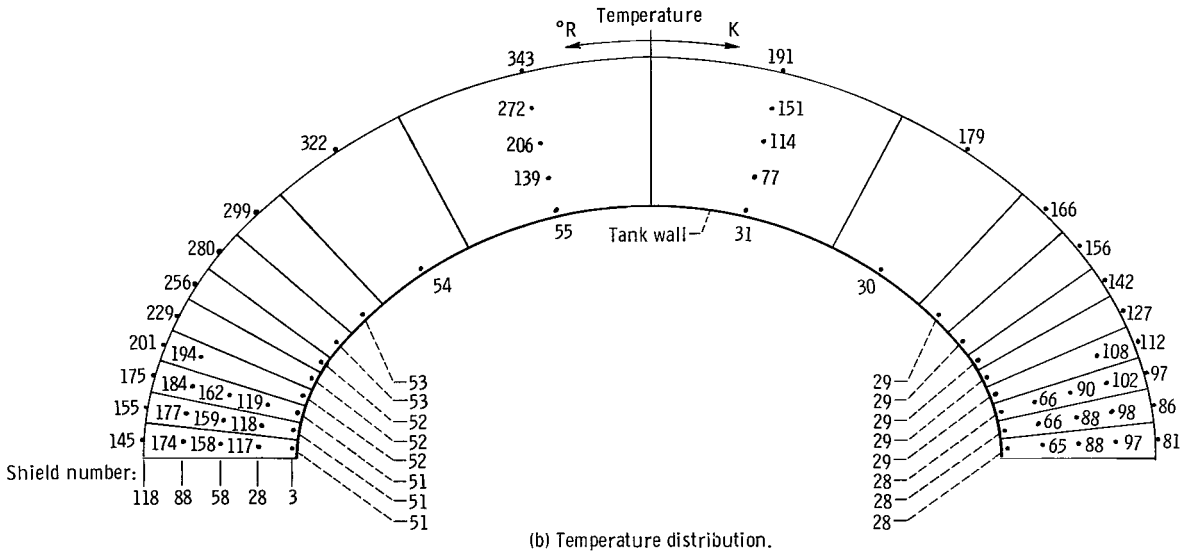

(b) Temperature distribution.

Figure 18. - Results of analysis for constant multilayer insulation (MLI) thickness using effective normal thermal conductivity representing an experimental average; no high-lateral-thermal-conductivity shields or targeting. Untargeted MLI emissivity, 0.024; payload emissivity, 0.11.

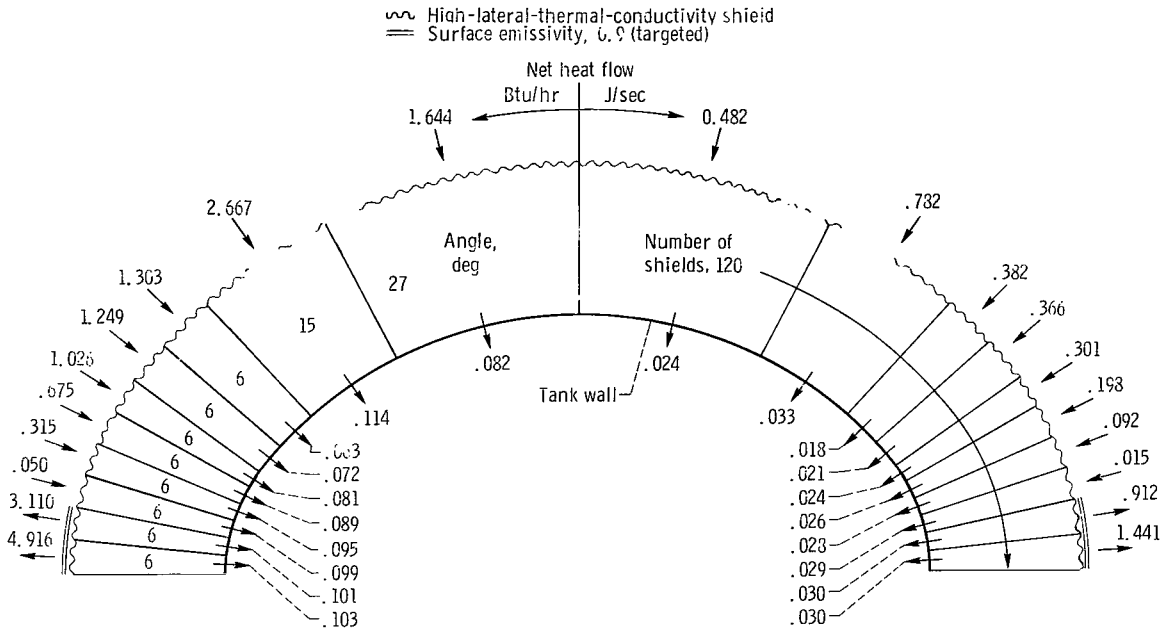

(a) Net heat flows across segment boundaries; total net heat flow, 0.903 Btu per hour (0.265 J/sec).

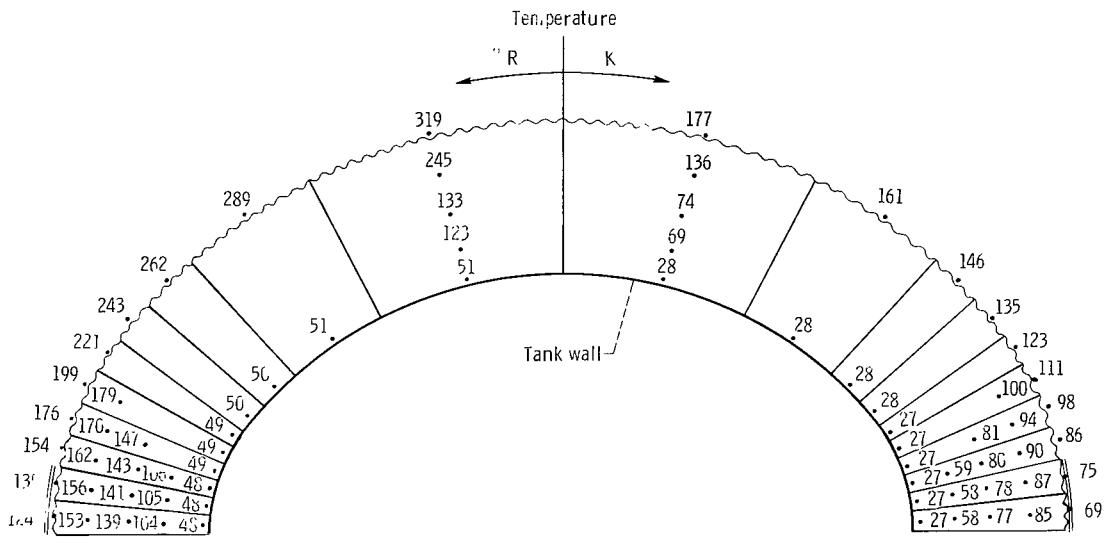

(b) Temperature distribution.

Figure 19. - Results of analysis for constant multilayer insulation (MLI) thickness using effective normal thermal conductivity representing an experimental average; high-lateral-thermal-conductivity shield at surface and targeting last two segment surfaces. Untargeted MLI surface emissivity, 0.024; payload emissivity, 0.11.

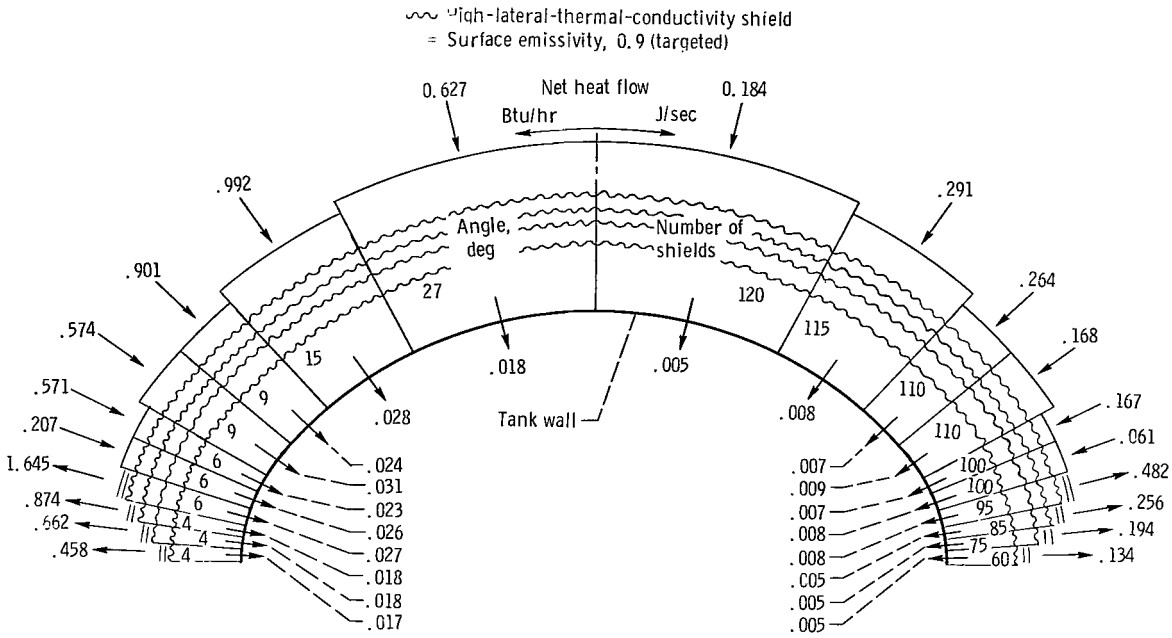

(a) Net heat flows across segment boundaries; total net heat flow, 0.231 Btu per hour (0.068 J/sec).

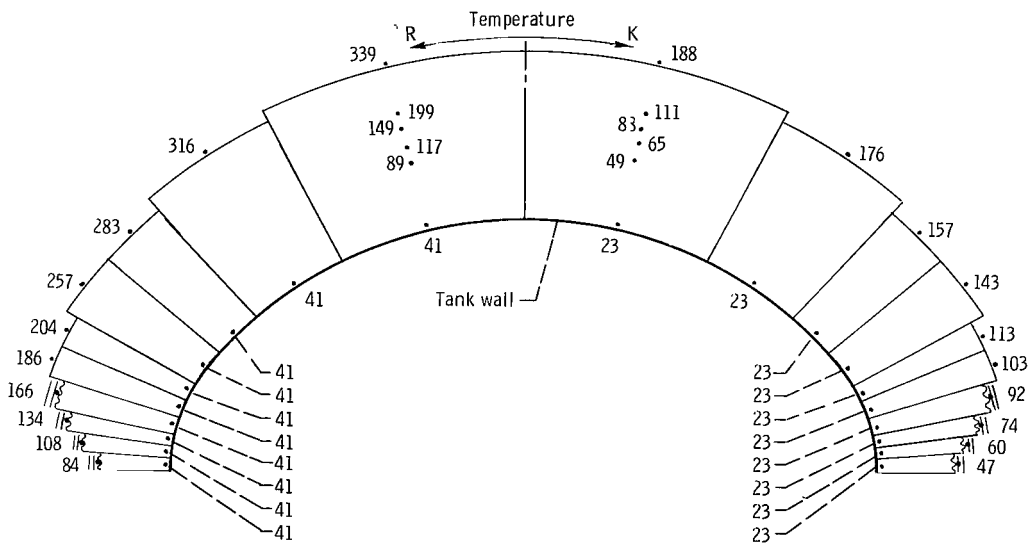

(b) Temperature distribution.

Figure 20. - Results of analysis for optimum customized multilayer insulation (MLI) configuration using effective normal thermal conductivity representing an experimental average. Untargeted MLI surface emissivity, 0.024; payload emissivity, 0.11.

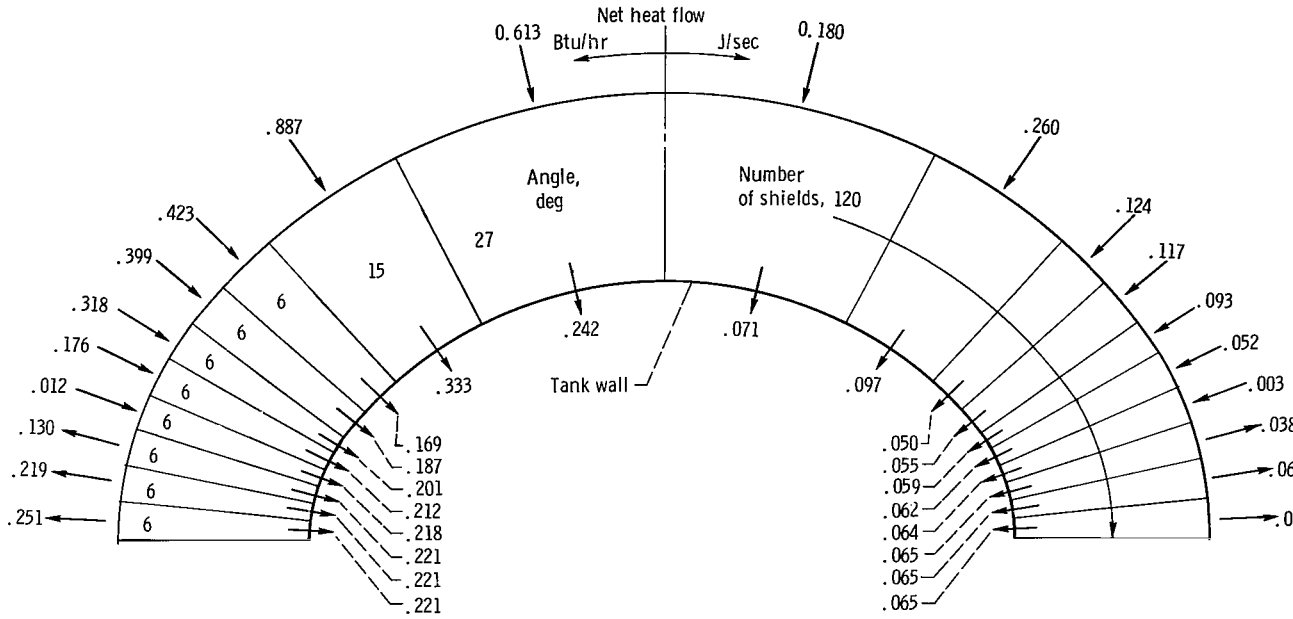

(a) Net heat flows across segment boundaries; totat net heat flow, 2.226 Btu per hour (0.652 J/sec).

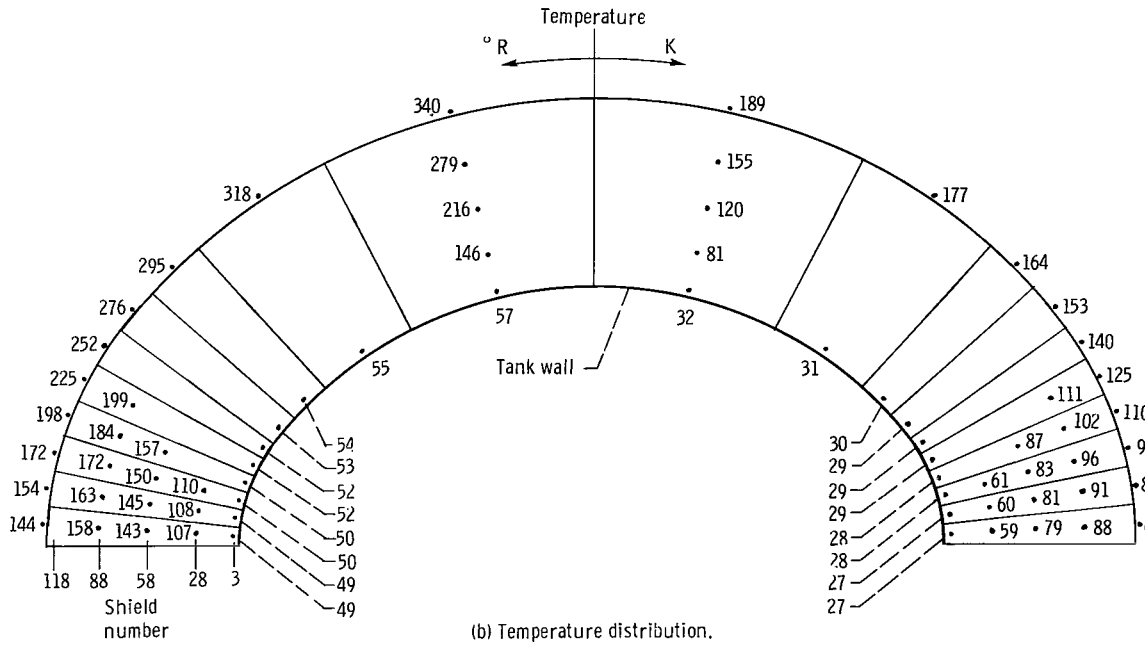

(b) Temperature distribution.

Figure 21. - Results of analysis for constant multilayer insulation (MLI) thickness using effective normal thermal conductivity representing a value twice experimental average; no high-lateral-thermal-conductivity shields or targeting. Untargeted MLI surface emissivity, 0.024; payload emissivity, 0.11.

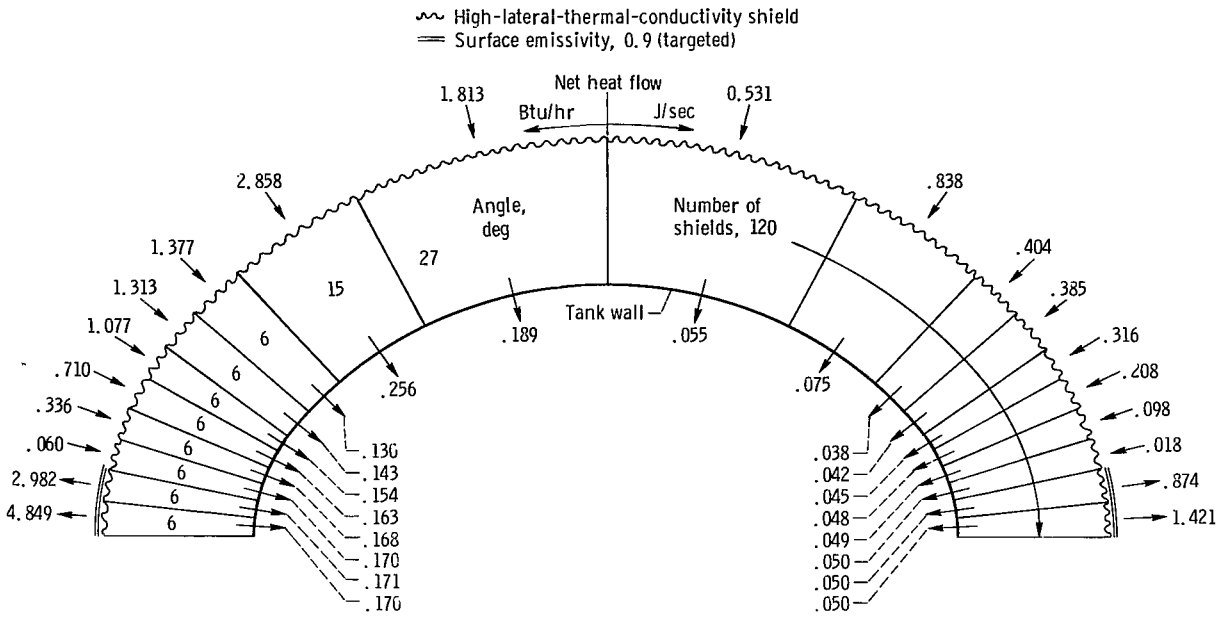

(a) Net heat flows across segment boundaries; total net heat flow, 1.714 Btu per hour (0.502 J/sec).

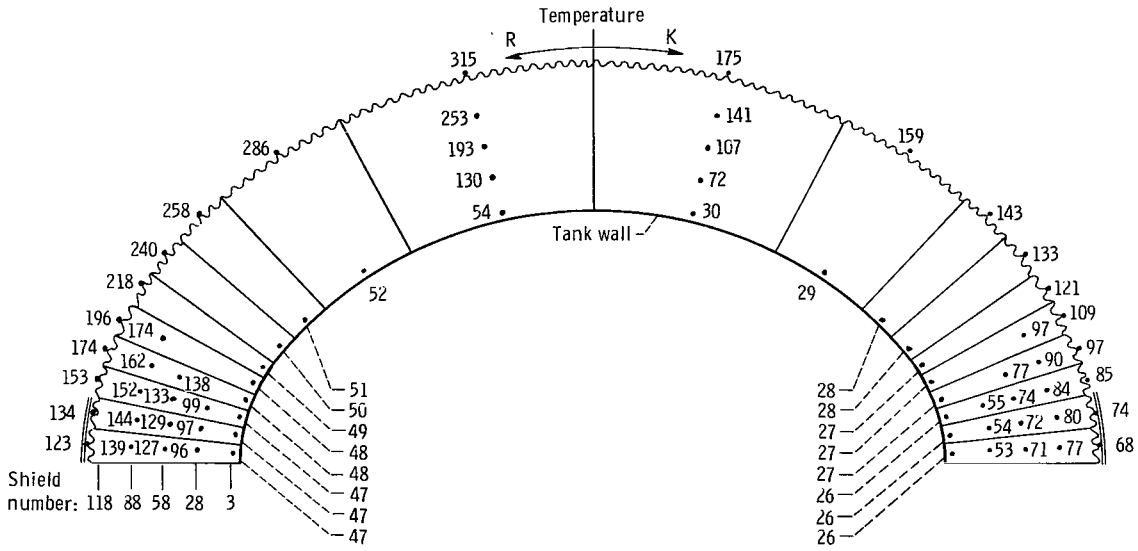

(b) Temperature distribution.

Figure 22. - Results of analysis for constant multilayer insulation (MLI) thickness using effective normal thermal conductivity representing value twice experimental average; high-lateral-thermal-conductivity shield at surface and targeting last two segment surfaces. Untargeted MLI surface emissivity, 0.024; payload emissivity, 0.11.

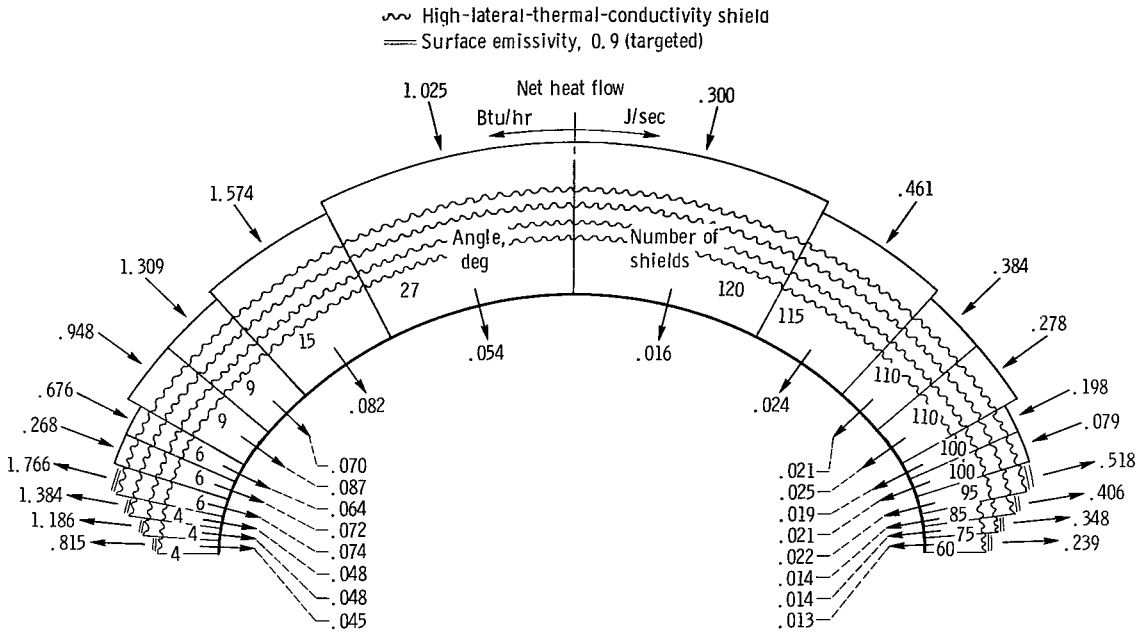

(a) Net heat flows across segment boundaries; total net heat flow, 0.647 Btu per hour (0.190 J/sec).

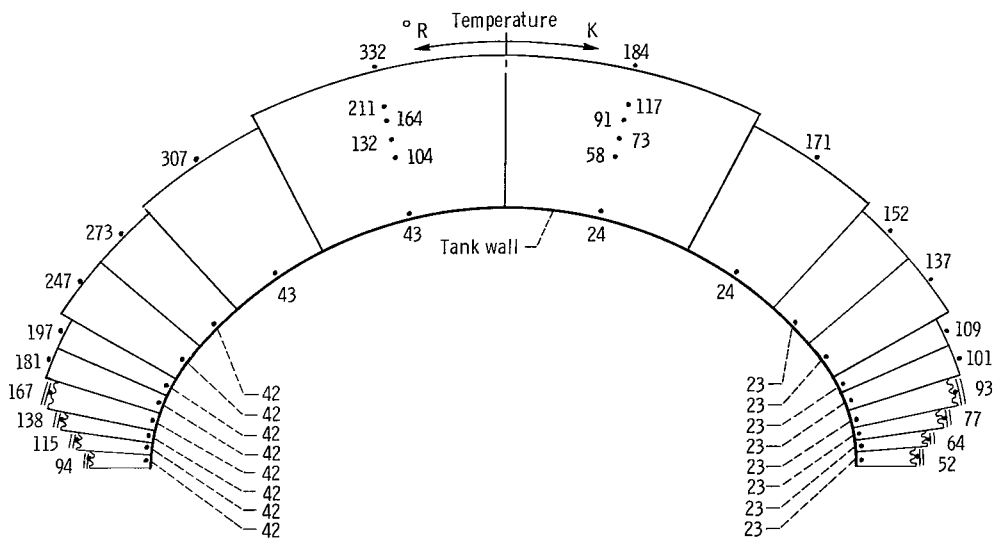

(b) Temperature distribution.

Figure 23. - Results of analysis for optimum customized multilayer insulation (MLI) configuration using effective normal thermal conductivity representing a value twice experimental average. Untargeted MLI surface emissivity, 0.024; payload emissivity, 0.11.

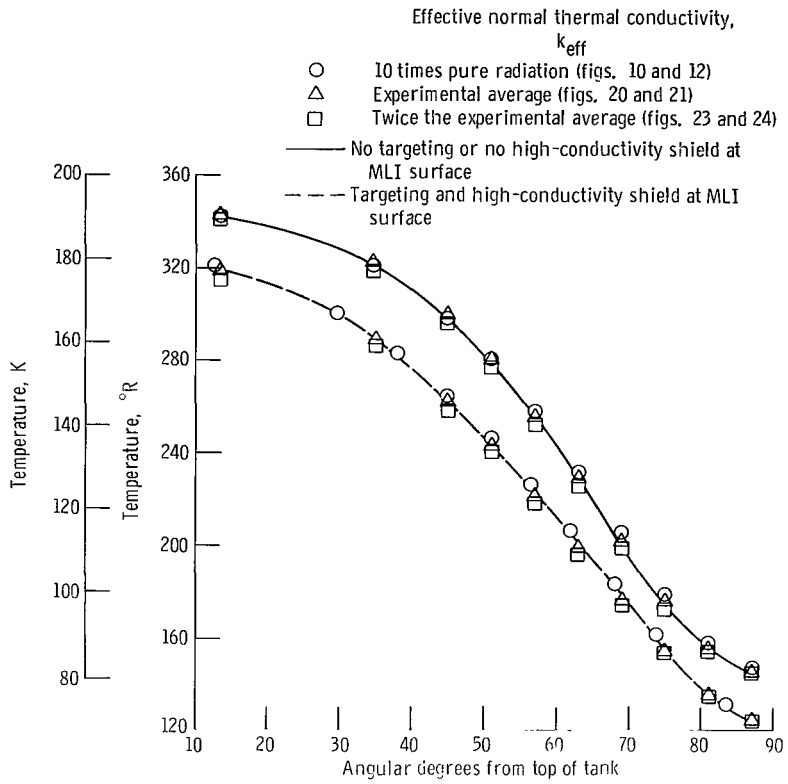

Figure 24. - Multilayer insulation (MLI) surface temperature profiles for constant MLI thickness (120 shields) with and without surface shield being targeted and of high lateral thermal conductivity.

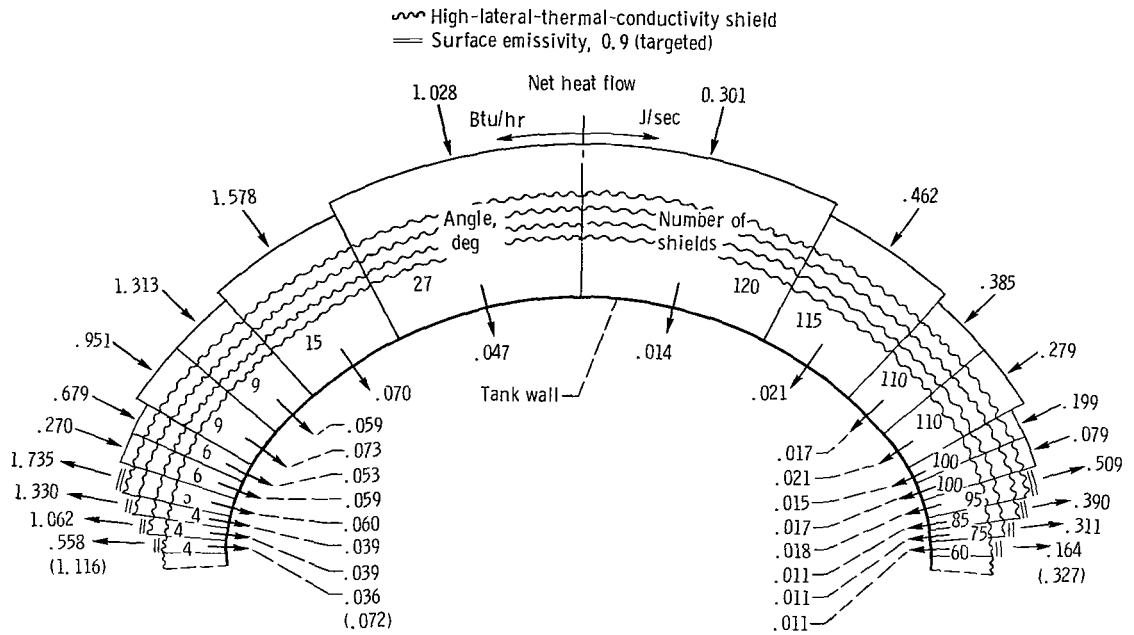

(a) Net heat flows across segment boundaries; total net heat flow, 0.535 Btu per hour (0.157 J/sec).

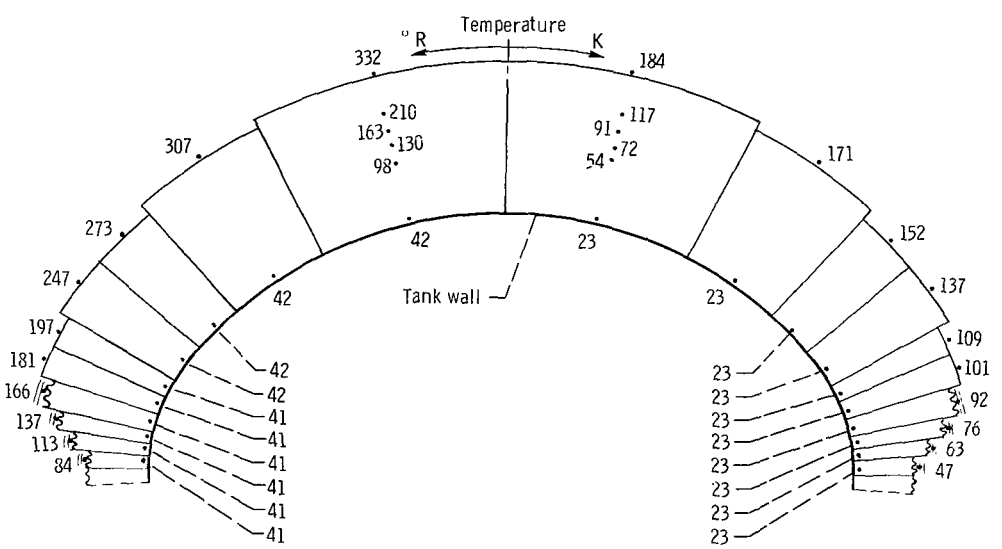

(b) Temperature distribution.

Figure 25. - Results of analysis for optimum customized multilayer insulation configuration shown in figure 23 when last segment area is doubled.

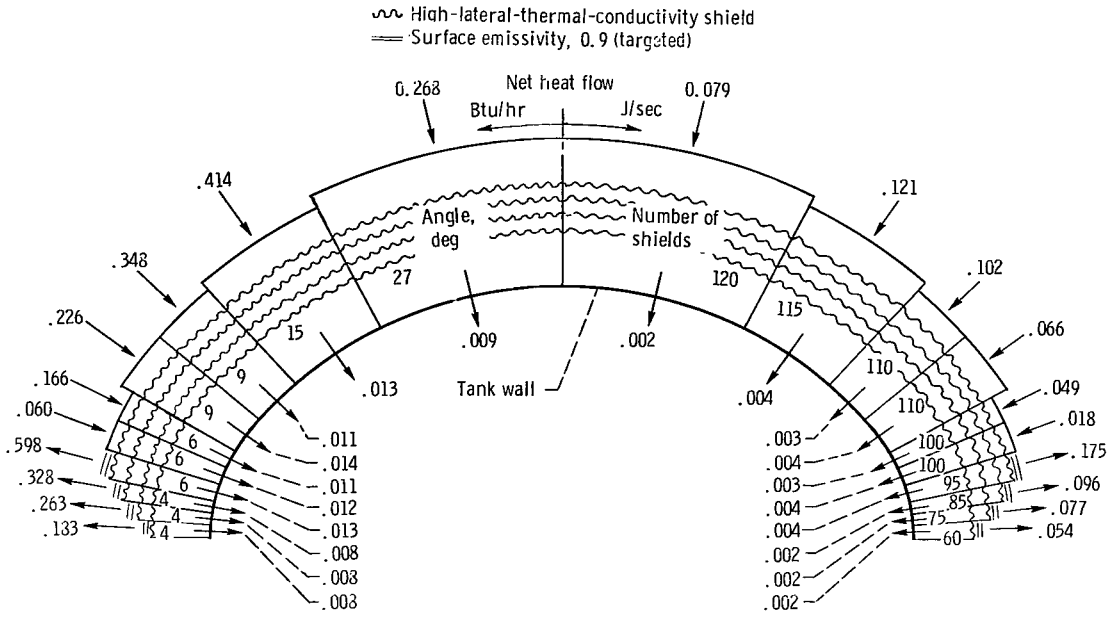

(a) Net heat flows across segment boundaries; total net heat flow, 0.109 Btu per hour (0.032 J/sec).

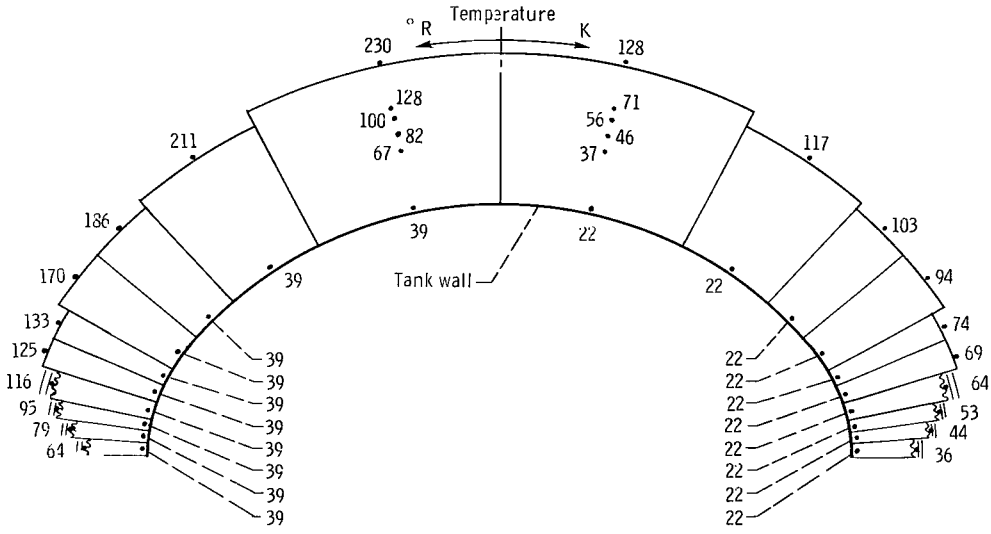

(b) Temperature distribution.

Figure 26. - Results of analysis for optimum customized multilayer insulation (MLI) configuration using effective normal thermal conductivity representing an experimental average when payload emissivity is 0.024. Untargeted MLI surface emissivity, 0.024.

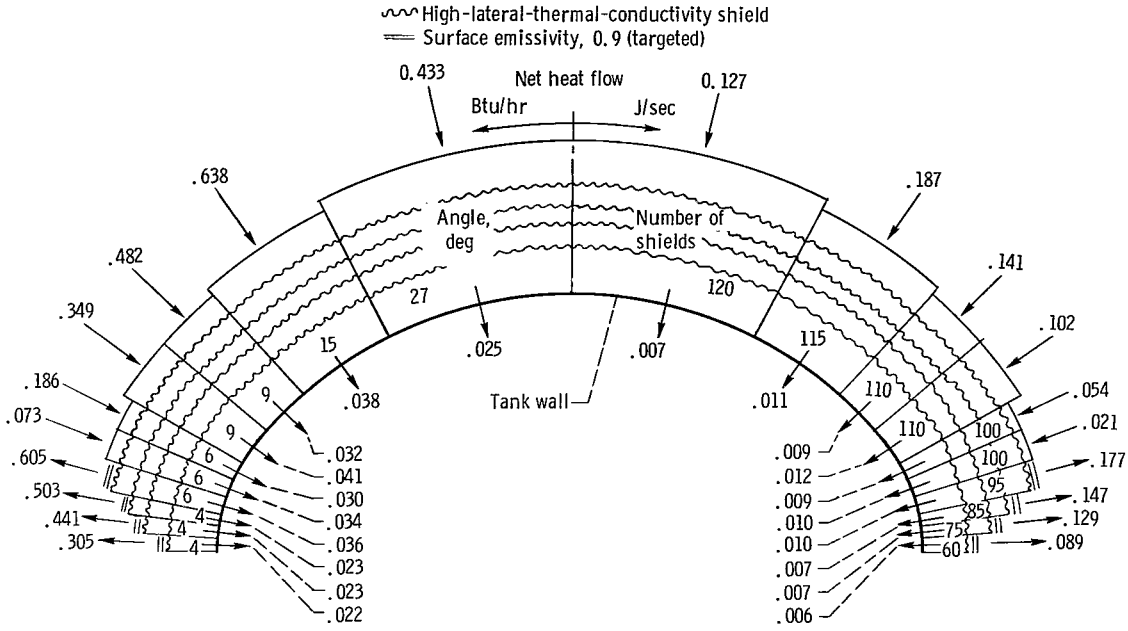

(a) Net heat flows across segment boundaries; total net heat flow, 0.306 Btu per hour (0.090 J/sec).

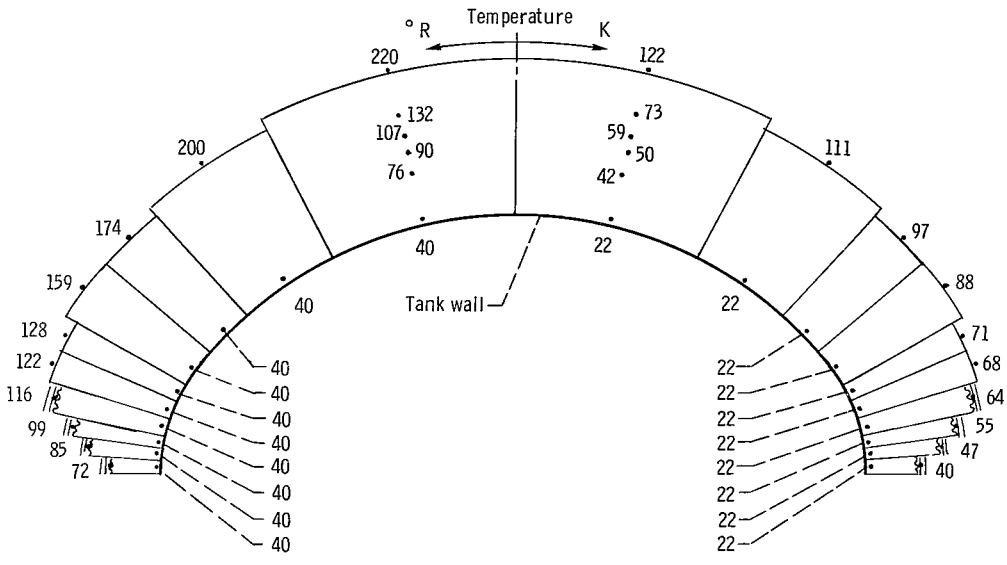

(b) Temperature distribution.

Figure 27. - Results of analysis for optimum customized multilayer insulation (MLI) configuration using effective normal thermal conductivity representing a value twice experimental average when payload emissivity is 0.024. Untargeted MLI surface emissivity, 0.024.

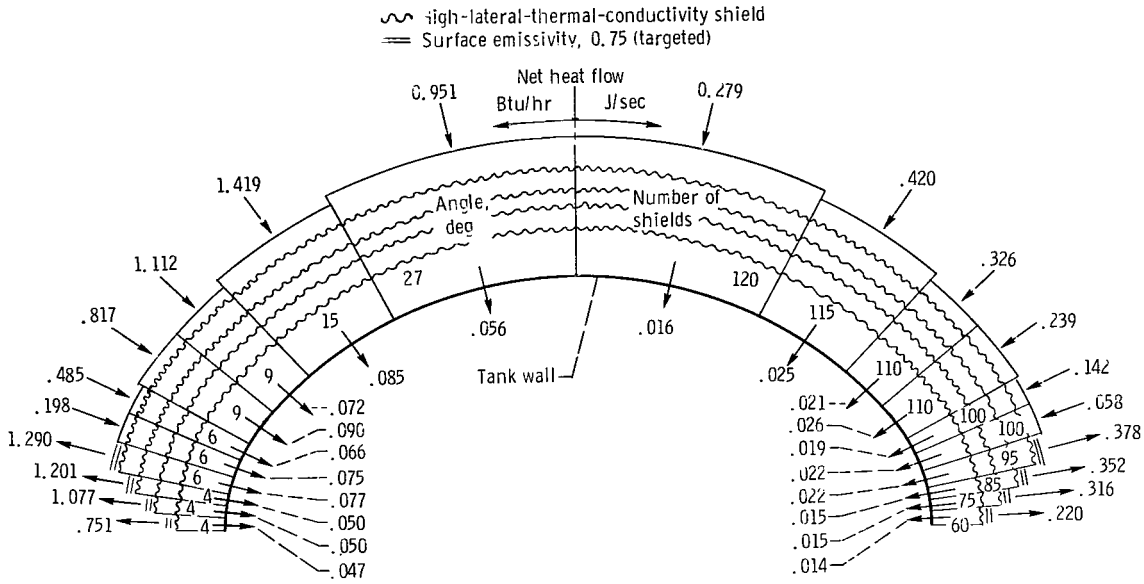

(a) Net heat flows across segment boundaries; total net heat flow, 0.667 Btu per hour (0.196 J/sec).

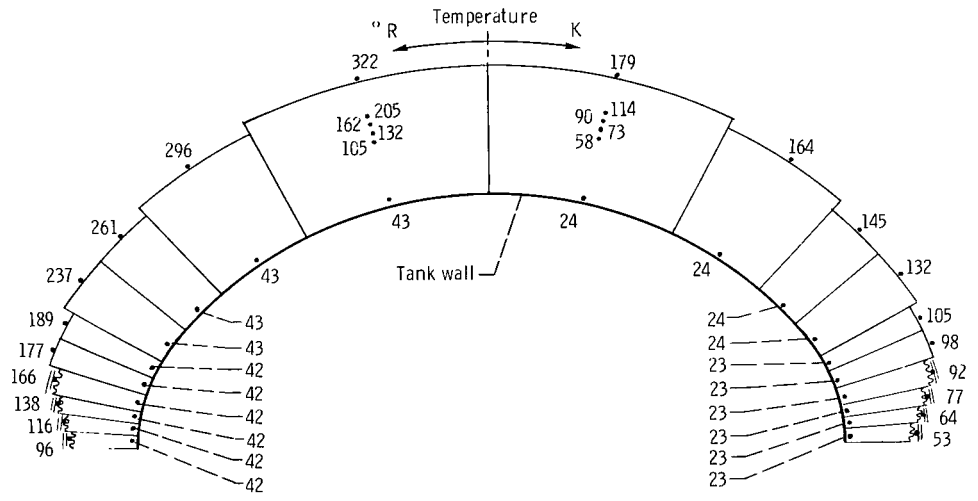

(b) Temperature distribution.

Figure 28. - Results of analysis for optimum customized multilayer insulation (MLI) configuration using effective normal thermal conductivity representing a value twice experimental average except targeted surface emissivity is 0.75 and untargeted surface emissivity is 0.015. Payload emissivity, 0.11.

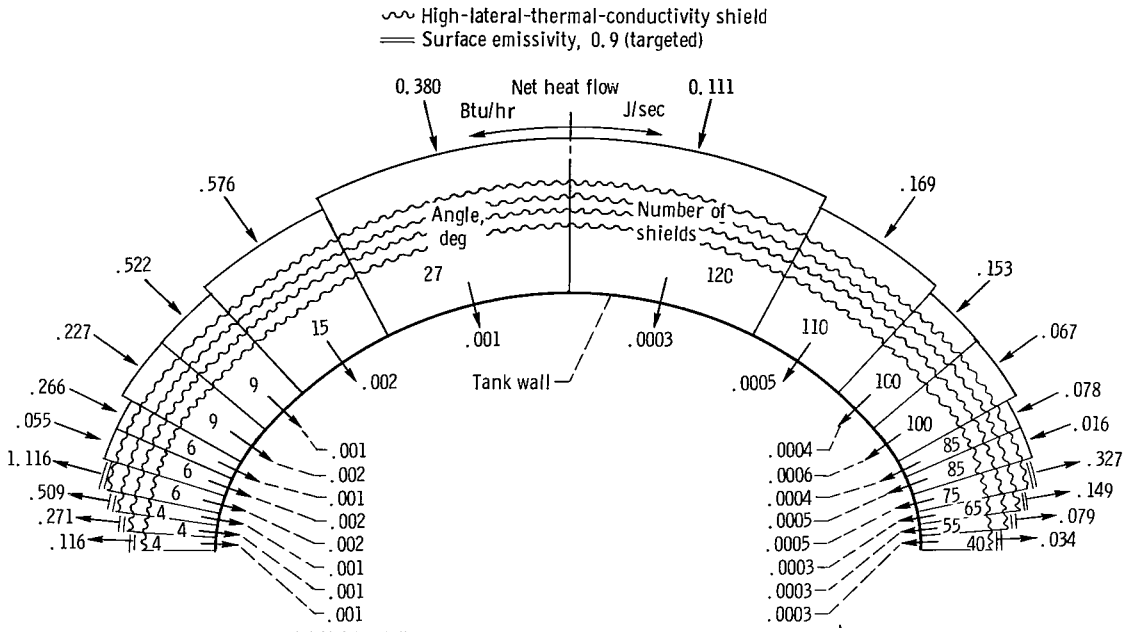

(a) Net heat flows across segment boundaries; total net heat flow, 0.013 Btu per hour (0.004 J/sec).

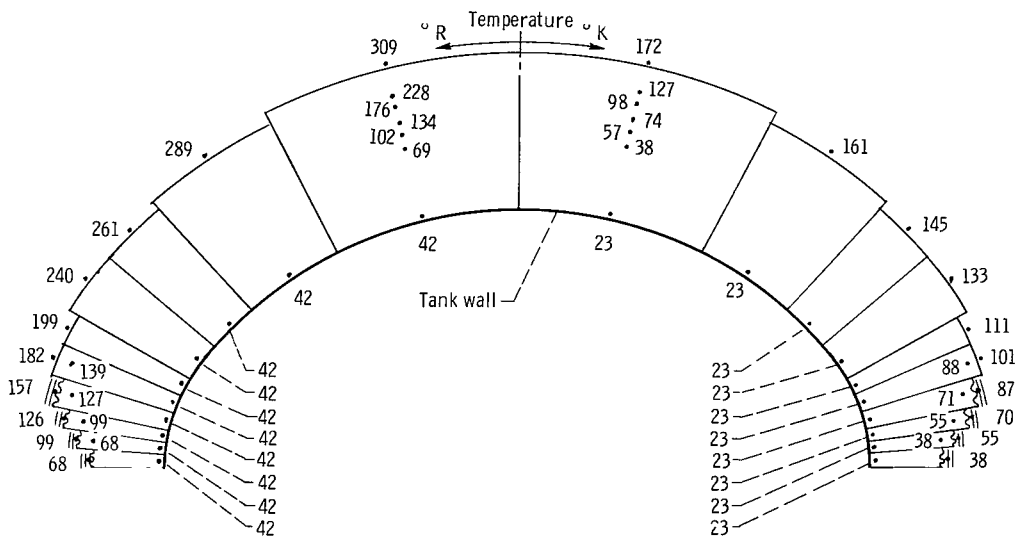

(b) Temperature distribution.

Figure 29. - Results of analysis for optimum customized multilayer insulation (MLI) configuration using effective normal thermal conductivity of 10 times pure radiation except tank-payload spacing doubled. Untargeted MLI surface emissivity, 0.024; payload emissivity, 0.11.

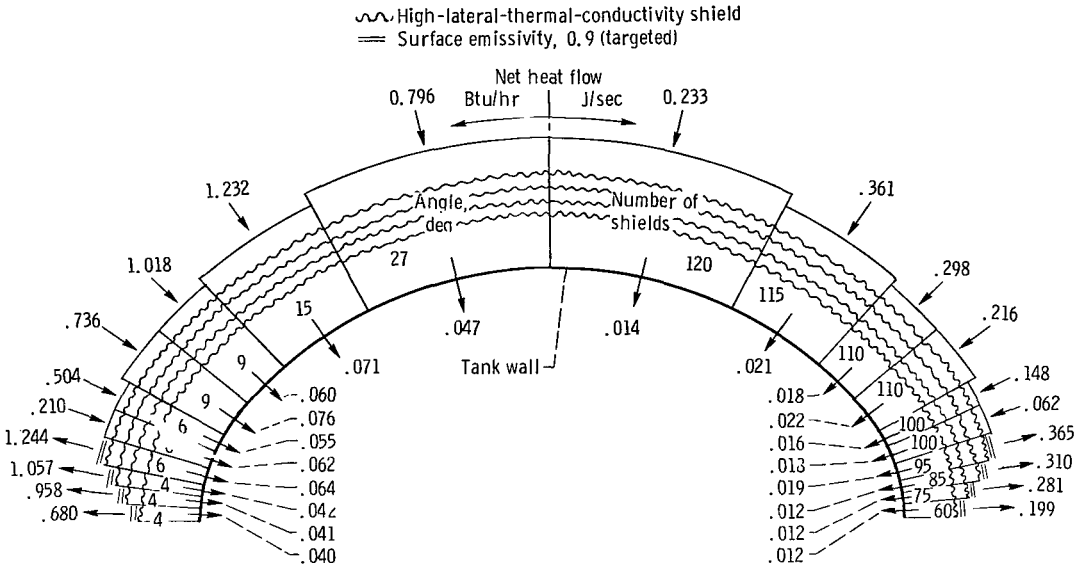

(a) Net heat flows across segment boundaries; total net heat flow, 0.558 Btu per hour (0.163 J/sec).

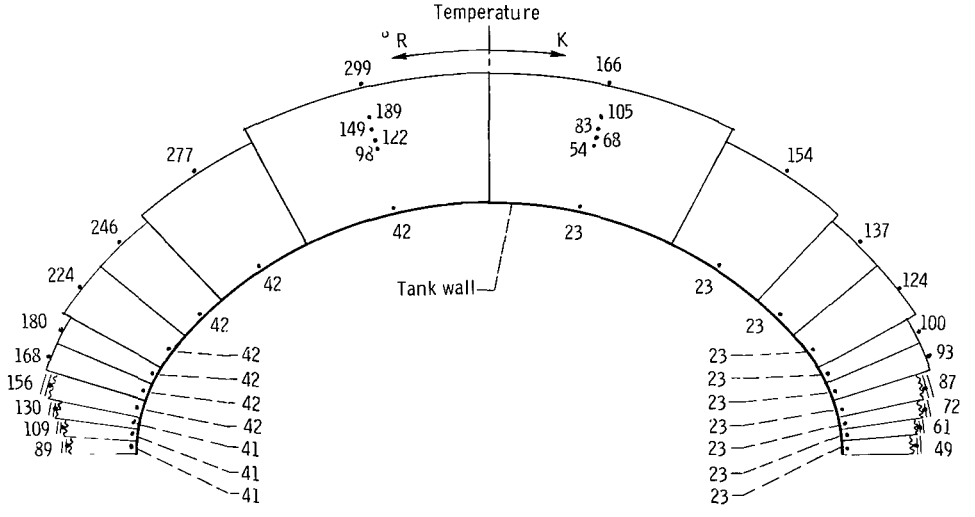

(b) Temperature distribution.

Figure 30. - Results of analysis for optimum customized multilayer insulation (MLI) configuration using effective normal thermal conductivity representing a value twice experimental average except tank-payload spacing doubled. Untargeted MLI surface emissivity, 0.024; payload emissivity, 0.11.

NATIONAL AERONAUTICS AND SPACE ADMINISTRATION
WASHINGTON, D.C. 20546

OFFICIAL BUSINESS
PENALTY FOR PRIVATE USE $300

FIRST CLASS MAIL

POSTAGE AND FEES PAI
NATIONAL AERONAUTICS
SPACE ADMINISTRATION

06U 001 52 51 3DS 71043 00903
AIR FORCE WEAPONS LABORATORY /WLOL/
KIRTLAND AFB, NEW MEXICO 87117

ATT E. LOU BOWMAN, CHIEF,TECH. LIBRARY

POSTMASTER: If Undeliverable (Section 1
Postal Manual) Do Not Ret

"The aeronautical and space activities of the United States shall be conducted so as to contribute . . . to the expansion of human knowledge of phenomena in the atmosphere and space. The Administration shall provide for the widest practicable and appropriate dissemination of information concerning its activities and the results thereof."

—NATIONAL AERONAUTICS AND SPACE ACT OF 1958

NASA SCIENTIFIC AND TECHNICAL PUBLICATIONS

TECHNICAL REPORTS: Scientific and technical information considered important, complete, and a lasting contribution to existing knowledge.

TECHNICAL NOTES: Information less broad in scope but nevertheless of importance as a contribution to existing knowledge.

TECHNICAL MEMORANDUMS: Information receiving limited distribution because of preliminary data, security classification, or other reasons.

CONTRACTOR REPORTS: Scientific and technical information generated under a NASA contract or grant and considered an important contribution to existing knowledge.

TECHNICAL TRANSLATIONS: Information published in a foreign language considered to merit NASA distribution in English.

SPECIAL PUBLICATIONS: Information derived from or of value to NASA activities. Publications include conference proceedings, monographs, data compilations, handbooks, sourcebooks, and special bibliographies.

TECHNOLOGY UTILIZATION PUBLICATIONS: Information on technology used by NASA that may be of particular interest in commercial and other non-aerospace applications. Publications include Tech Briefs, Technology Utilization Reports and Technology Surveys.

Details on the availability of these publications may be obtained from:

SCIENTIFIC AND TECHNICAL INFORMATION OFFICE

NATIONAL AERONAUTICS AND SPACE ADMINISTRATION

Washington, D.C. 20546